INFORMATION TO USERS

This manuscript has been reproduced from the microfilm master. UMI films the text directly from the original or copy submitted. Thus, some thesis and dissertation copies are in typewriter face, while others may be from any type of computer printer.

The quality of this reproduction is dependent upon the quality of the copy submitted. Broken or indistinct print, colored or poor quality illustrations and photographs, print bleedthrough, substandard margins, and improper alignment can adversely affect reproduction.

In the unlikely event that the author did not send UMI a complete manuscript and there are missing pages, these will be noted. Also, if unauthorized copyright material had to be removed, a note will indicate the deletion.

Oversize materials (e.g., maps, drawings, charts) are reproduced by sectioning the original, beginning at the upper left-hand corner and continuing from left to right in equal sections with small overlaps.

ProQuest Information and Learning
300 North Zeeb Road, Ann Arbor, MI 48106-1346 USA
800-521-0600

Application of some Hydraulic Principles to Flow Measurement

Chao Zhai

A Thesis

in the Department of

Building, Civil and Environmental Engineering

Presented in Partial Fulfillment of the Requirements

For the Degree of Master of Applied Science in Civil Engineering at

Concordia University

Montreal, Quebec, Canada

April 2003

Abstract

Application of some Hydraulic Principles to Flow Measurement

Chao Zhai

For flow near the end section of a trapezoidal channel, the velocity distribution is non-uniform and the streamlines are curved. These effects can be included using hydraulic principles in the formulation of the governing equations to obtain a very accurate relation between the channel discharge rate and the end depth.

At the end section of the overfall, the streamline pattern in the vertical plane of channel symmetry can be determined using the measured axial velocity data and the water surface profiles. The streamline pattern permits the evaluation of the streamline curvature, which in turn yields the curvature correction required to obtain the true static pressure profile at the end section. The directly determined pressure distribution agrees well with the predicted pressure distribution for the end section. In the region above the maximum velocity point near the end depth, energy relationships determined on the basis of the measured velocity and pressure field data confirm the fact that the total energy is essentially constant. The pressure head coefficient at the end section is a dominant parameter that influences the relationship between the channel discharge and the end depth.

Single slit weirs have been recently investigated to show that small discharge rates can be measured accurately by them. This concept has been applied to the flow through multislit weirs. This can extend the capacity of the slit weirs to measure accurately both low and high discharge rates. For this purpose the hydraulic concept of images is used to form a bank of slit weirs whose flow characteristics are essentially similar to the single weir. In a

multislit weir system consisting of an odd number of slit weirs. the weirs on either side of the central weir can be considered to be images of the central weir. The dependence of the discharge coefficient of multislit weirs on Reynolds number is shown to be the same as that for a single slit weir when the ratio b/B for single weirs is replaced by the ratio (nb)/B. For Reynolds number R_e less than 30000, R_e is the dominant parameter that determines the discharge coefficient for multislit weirs as in the case of single slit weirs. The multislit weir can accurately measure both very low and very large discharge.

Acknowledgements

I wish to thank Dr. A. S. Ramamurthy for suggesting the research topic. The help provided by Dr. Diep Vo and Mr.J. Qu during the initial period of the study is thankful acknowledged. Thanks are also due to Mr. N. Lang. Lastly; I would like to dedicate this work to my wife, Jianhua, for her best understanding and support.

Table of Contents

List of Notations

1. End depth

b = channel base width;

c = subscript denoting critical condition;

E = total energy;

e = subscript denoting end condition;

Q = flow rate;

r= radius of streamline curvature;

F= horizontal force;

$\mathbf{F}_0$ = upstream Froude number;

g = the gravitational acceleration;

h_s = static pressure head;

k = pressure coefficient;

K = pressure coefficient;

M = channel side slope;

u = axial velocity;

v = vertical velocity;

V = mean velocity;

w = lateral velocity;

x = distance from end section along channel axis;

y = vertical depth above the channel floor;

y_e = end depth;

y_c = critical depth;

$\bar{y}$ = the distance from the surface to the centroid of the water area;

z = lateral distance from channel axis;

Z = datum head;

β = momentum coefficient;

ρ = fluid density;

ψ = streamline function;

1,2 = subscripts denoting adjacent streamlines;

0 = subscript denoting upstream conditions

er,et = subscripts denoting the reference to the rectangular and triangular areas of the end depth section

2. Multislit weir

B channel width;

b weir width;

C_d discharge coefficient;

g gravitation acceleration;

h weir head;

n active slit number;

N total slit number;

P weir height;

R Reynolds number;

W Weber number;

γ specific weight;

ρ water density;

μ viscosity;

σ surface tension;

δ^* boundary- layer thicker;

List of Figures

List of Tables

Chapter1

Introduction and literature review

1.1 General remarks

The efficient management of water supplies is important as demand for water by the world's increasing population increases as new source of water become hard to find. One should conserve water by reducing wastage by efficient management. Regulation and control are the key factors in the management of available water resource. The present study is related to the adopted well-known hydraulic principles to improve the accuracy of prediction and extend the range of flow measurement in open channel. To this end, the commonly used measuring devices namely the end depth and rectangular weir are chosen for the study. A brief survey of investigations related to both the end depth study and the study of rectangular weirs applied to slit weirs is included below.

1.2 End depth flow

The flow depth y_e at the brink or end section of an open channel (Fig.2.1 and Fig.2.2) forming a free overfall has a unique relationship with the channel discharge rate Q. This fact is exploited by engineers to use the free overfall as a measuring device. The overfall is easy to construct and maintain. The term end depth ratio (EDR) denotes the ratio of the end depth y_e to the critical depth y_c.

The free overfall in a rectangular channel has been extensively studied by Rouse (1936), Fathy and Mahmoud. Shaarawi (1954), Delleur (1956), Rajaratnam and Muralidhar

(1968), Rajaratnam.et.al. (1976), Bauer and Graf (1971), Ali and Sykes (1972), and Terzidis (1985). The EDR in circular, and triangular channels has been studied by Diskin (1961), Rajaratnam and Muralidhar(1964A, B), Ali and Sykes (1972).

Hager (1983) applied extended energy and momentum equations to the flow near an overfall and derived an elegant expression relating EDR and the upstream Froude number. He also presented an expression for the surface profile near the brink section in a rectangular channel.

Studies on the free overfall in a trapezoidal channel are relatively few. Diskin (1961) performed the earliest theoretical and experimental investigation. Very good discussions of his work have been presented by Rajaratnam (1962), Hamid (1962) and Replogle (1962).

In most studies, the pressure force at the end section is neglected and the momentum coefficient β is assumed to be unity in the final analysis. The pressure coefficient K for the end depth problem can be defined as the ratio of the pressure force based on actual end depth pressure distribution to the pressure force based on hydrostatic pressure distribution.

Keller and Fong (1989) studied the trapezoidal free overfall experimentally and theoretically considering the trapezoidal section is a combination of a rectangular and a triangular section involving a nonzero pressure distribution at the brink. Based on the

widely accepted measurements of Replogle (1962), they derived a sixth-degree equation linking the end depth to the critical depth, which requires an iterative numerical solution. Terzidis and Anastasiadou-Partheniou (1990) studied the flow at the end section of a trapezoidal section using the test data of Replogle (1962) and Rajaratnam and Muralidhar (1964b). Their recommended equation is quadratic and hence it is easy to solve and practical to use. He derived a simple equation linking the end depth to the critical depth. Based on published experimental data, Gupta et al (1993) presented a calibration curve for the prediction of the discharge in a trapezoidal channel. Litsa Anastasiadou-Partheniou and Evangelos Hatzigiannakis (1995) accounted for the convergence of streamlines while arriving at the relationship between EDR and the Froude number in the upstream channel.

In the present study, the vertical distributions of the velocity components and the static pressure head h, at the end section of a horizontal trapezoidal channel are directly determined to obtain the momentum coefficient β and the pressure coefficient K. The information obtained about β and K is used to estimate the relative importance of these coefficients in the formulation of the momentum equation. Based on the measured velocity data near the end depth section, the streamline pattern is determined in the vertical plane of channel symmetry. This in turn, yields the streamline curvature correction needed to rectify the hydrostatic pressure head distribution at the end depth section. Lastly, energy relationships determined in the vertical plane through the channel axis near the end section confirm the fact that the total energy is essentially constant for the flow field, in the region above the maximum velocity point.

1.3 Rectangular weir flow

Rectangular weirs:

The rectangular sharp-crested weir serves as a simple and accurate device for flow measurement in open channels (Fig.3.4, Fig.3.5). It also acts as a control section in an open channel. A large number of studies have been devoted to the problem of sharp-crested rectangular weirs in the past (Bos. 1989). Kindsvater and Carter (1957) presented a comprehensive solution for the weir discharge characteristics based on dimensional analysis and the studies of other investigators. On the basis of their experimental results, Kandaswamy and Rouse (1957) identified two distinct ranges for the flow over rectangular sharp-crested weir in terms of parameter $\frac{h}{P}$. For potential flow over a rectangular sharp-crested weir, several theoretical solutions have been proposed. Sarginson (1972) experimentally and theoretically determined the discharge coefficient C_d of the sharp crested weir as a simple function of the Weber number. Han and Chow (1981) investigated the characteristics of relatively high sharp-crested weirs through hodograph transformations. Experimental data related to velocity and pressure distribution data have been used to predict a relationship between the discharge coefficient C_d and h/p for sharp-crested rectangular weirs (Ramamurthy 1987).

Slit weirs:

Aydin (1999) introduced the concept of the slit weir, which was a narrow rectangular sharp edge weir capable of measuring very low flow rates. He showed that the slit weir discharge coefficient C_d is a function of R_e in the range of the test variables covered in his experiments. According to him,

$$C_d = 0.562 + 11.35 / R_e^{0.5} \qquad (1.1)$$

The slit weir is an efficient device to measure very low flow rates. To permit the slit weir to measure a wide range of flow rates, one can use a bank of identical slit weirs in which each weir is an image of the neighboring weir. This interpretation is permitted, as the dividing streamline between two adjacent weirs can be replaced by a solid boundary (Fig.3.3). In the present study, this simple concept is used to predict the flow characteristics of multislit weirs capable of measuring a very wide range of flow rates. This is achieved by blocking appropriate weirs to suit the low flow rate selected. Accordingly, for the system of N multislit weirs in which n weirs are active (not blocked), the effective weir width ratio is (nb)/B.

In the present tests, (nb)/B is varied from 0.0083 to 0.175. Consequently, for these (nb)/B values, the corresponding theoretical contraction coefficient for flow past a two-dimensional slit is close to 0.61 (Olson 1968). The range of dimensional parameters chosen for the tests is shown in table 3.1.

For the slit weirs A1, B1 and C1 (Fig.3.3) of the three multislit weir unit (n = 3) set in the channel of width B, the streamlines EF, GH, IJ and KL are also the stagnation streamlines. As such, the streamlines GH and IJ can be replaced by solid boundaries.

Consequently, the slit weirs A1 and C1 can be considered to be images of the slit weir B1. Theoretically the three weirs A1, B1 and C1 can be viewed as identical single weirs whose effective width ratio is $3b/B$. This procedure was adopted while analyzing the 3, 7 and 15 unit multislit weirs. However in practice, the slightly non-uniform distribution of the approach velocity in the main channel will result in slightly difference in the flow through the individual multislit weirs.

1.4 Scope of present study

The present study is mostly experimental and the analysis is limited to the interpretation of test data collected.

For the end depth study, the objectives are listed below:

(1) To determine the total energy relationship for flow near the end depth and show that the total energy outside the maximum velocity point of the boundary layer flow near the end depth is nearly constant.

(2) To determine the streamline equations for flow in the neighborhood of end depth to obtain the curvature corrections and predict the true static pressure.

(3) To determine the pressure coefficient K and momentum coefficient β and to use them in the momentum equation to obtain an accurate relationship between Q and y_e.

(4) To validate the predicted Q-y relation using present and existing data.

For the second part of study dealing with multislit weirs, the objectives are listed below:

(1) To validate the concept of treating weirs on either side of central weir of the multislit weirs to be image weirs of the central weir.

(2) To extend the range of discharge measured by multislit weirs.

(3) To determine flow and geometric parameters which influence the discharge of multislit weirs.

1.5 Thesis outline

This thesis is divided into four chapters, inclusive of this chapter that provides an introduction to the study and the existing literature related to it.

In chapter 2, end depth method study is presented. This study covers the end depth method, theoretical analysis, experimental set up and the discussion of results.

The study of the rectangular weir flow and its adoption to slit weirs and multislit weirs is presented in chapter 3. This chapter includes the weir concept, the equipment and experimental procedure to study multislit weirs and the discussion of results.

Chapter 4 deals with conclusions and suggestions for future studies of both the end depth study and the multislit weirs study.

Chapter 2

End depth

This chapter deals with the end depth study and the application of the pressure correction for curvilinear flow at the end depth to obtain reliable relations between the end depth and the channel discharge.

2.1General

Past theoretical and experimental investigations have demonstrated that a relationship exists between the flow rate and the depth at the end section of a channel. Such a relationship enables in principle the use of a free overfall as a discharge measuring structure. Flow rate is a function of the critical depth y_c in the channel and hence the ratio of the end depth y_e to the critical depth y_c (EDR) is a significant parameter. It is desirable to set up a simple and accurate EDR as a convenient measuring device. Studies of EDR problems focused on the two aspects: one is the determination of EDR; another is the assumption analysis. In practice, the end depth method for determining the discharge is very useful since channels can be easily modified to have a free overfall, and natural channels often have this configuration. The problem of EDR as a discharge-measuring device has attracted considerable interest.

2.2 Theoretical considerations

2.2.1 End depth pressure

Near the end section, the profile has a substantial curvature and the pressure distribution is nonhydrostatic. Streamline curvature produces acceleration components normal to the flow direction and hence, the pressure distribution deviates from the hydrostatic distribution. At the end section, the vertical components of the normal acceleration are opposite to the gravitational acceleration; hence the curve for the actual pressure lies below the curve for the hydrostatic pressure distribution (Fig 2.1). The normal acceleration at any point near the end section is given by V^2/r, where V = mean velocity and r = radius of curvature of the streamline at that point. The governing equation is:

$$\frac{\partial p}{\partial y} + \gamma \cos\theta = \frac{\rho V^2}{r} \tag{2.1}$$

Where, γ is the specific weight of fluid, ρ is the density of fluid, θ is the channel slope. The static pressure head h_s corrected for curvature of the streamline at a depth y is,

$$h_s = y - \frac{1}{g}\int_y^0 \frac{V^2}{r} dy \tag{2.2}$$

Here, g is the gravitational acceleration, y is the depth above the channel floor (Fig 2.1).

2.2.2 Momentum equation for end depth flow

Eq. (2.3) denote the momentum equation in the horizontal direction

$$Q\beta\rho V_c - Q\rho V_c = F_c - F_e \tag{2.3}$$

$$F_c = K\gamma\bar{y}_c A_c = K_{cr}\gamma\bar{y}_{cr}A_{cr} + K_{ct}\gamma\bar{y}_{ct}A_{ct} \tag{2.3a}$$

$$F_c = \gamma \bar{y}_c A_c \qquad (2.3b)$$

Here, $\bar{y}$ = the distance from the surface to the centroid of the water area and K = pressure coefficient. Subscripts c and e denote respectively the critical depth and the end depth sections while, *er* and *et* denote the reference to the central rectangular area and the triangular areas of the end depth section in a trapezoidal channel.

To obtain the pressure force term on the right hand side of the momentum equation (Eq.2.3), the average pressure at the end section is needed. This is obtained by finding the average pressure head at each location A, B, C and D (Fig.2.3) using the static pressure head data recorded at the end section. The average pressure heads at these 4 locations are weighted considering their areas of influence (Fig.2.3). The resulting weighted average pressure is multiplied by the end section's flow area to obtain the horizontal pressure force term F_c at the end section.

The streamline at the end section is highly curvilinear. In order to evaluate the components, momentum coefficient β and the pressure coefficient K value must be determined. In the previous studies, β and K have not often been experimentally determined for the trapezoidal channel.

Due to the velocity variation in end section, the true momentum term at the end section is $\int \rho \cdot u^2 dA$.

$$\beta \cdot \rho \cdot Q \cdot V = \int \rho \cdot u^2 dA \qquad (2.4)$$

As $Q = V\ A$, Eq 2.4 yields the expression for β

$$\beta = \frac{\int u^2 dA}{V^2 A} \qquad (2.4a)$$

Similarly, the true kinetic energy flux through the end section in terms of the energy coefficient is:

$$\frac{\alpha \cdot \rho \cdot QV^2}{2} = \int \frac{\rho \cdot u^3}{2} dA \qquad (2.5)$$

Hence,

$$\alpha = \frac{\int u^3 dA}{V^3 A} \qquad (2.5a)$$

2.2.3 Using the energy equation to check the total energy outside of the boundary layer near the end depth

Outside the boundary layer, for the end depth flow, the total energy is nearly constant. Thus, in the vertical plane of channel symmetry,

$$\frac{v^2}{2g} + \frac{u^2}{2g} + \frac{w^2}{2g} + h_s = cons\tan t \qquad (2.6)$$

in which u = x direction velocity, v = y direction velocity, w = z direction velocity (Fig 2.6).

2.2.4 Determination of Streamlines

The axial and vertical velocity components u and v measured in the vertical plane of channel symmetry permit one to trace the streamlines in this plane. Near the end depth

section, u and v varied very little in the lateral direction except in the small boundary layer region near the solid surfaces. Along the plane of symmetry of the channel, the measured top water surface denotes the upper bounding streamline. The channel floor together with the bottom nappe denotes the lower bounding streamline. Four additional streamlines (Fig 2.4) are also obtained using the velocity survey data along the plane of channel symmetry. The streamlines equations are determined using the following facts.

1. In the plane of symmetry, the lateral velocity component w = 0
2. Except very near the solid boundary, the axial and vertical velocity components u and v are essentially constant in the lateral direction at sections H, I and J (Fig.2.4). Test data confirm this fact.
3. The constant discharge per unit depth dq passing between adjacent streamlines ψ_1 and ψ_2 is equal to $\mid \psi_2 - \psi_1 \mid$. The discharge dq between streamlines can be obtained by integrating the measured velocity profile data. Equal discharge passes between the adjacent streamlines.
4. Along the vertical plane of symmetry of the channel, the measured top water surface denotes the upper bounding streamline. The channel floor together with the bottom nappe denotes the lower bounding streamline. The value of ψ for the lower bounding streamline may be denoted as 0.
5. At any point along a streamline v/u = slope of streamline. This fact can be used to check the equation obtained for the streamline.

Using Eq.2.2 and the experimentally determined streamline equations (Fig.2.4), the curvature correction (Eq.2.2) needed to modify the hydrostatic pressure head distribution is obtained. Applying these corrections to the hydrostatic pressure head at different

elevations, the true static pressure head distribution at sections J, I and H (Fig.2.4) of the end section are predicted.

2.2.5 Determination of end depth pressure correction

Near the end depth section, the streamlines have a substantial curvature and the pressure distribution is nonhydrostatic. Streamline curvature produces appreciable acceleration components normal to the flow direction. The pressure distribution deviates from the hydrostatic if curvilinear flow occurs in a vertical plane. In order to get the end depth pressure correction, from the governing equation

$$H = y_s - \frac{1}{g \cdot} \int_{y_s}^{0} \frac{V^2}{r} dy \qquad (2.7)$$

The radius of the streamline and three-dimension velocity should be determined firstly. Compared with u and v, w velocity is very small, hence we can take the end depth flow as the two-dimensional. The stream function relation are given below:

$$\psi = u \cdot dy - v \cdot dx \qquad (2.8)$$

in which ψ =stream function

u =flow direction velocity

v =vertical direction velocity

The surface streamline was measured by the point gage.

After the streamline equation was obtained, the streamline radius at the end section can be found. Following this, the pressure head correction can be determined by the following formula:

$$r = \frac{(1+(\frac{dy}{dx})^{\frac{3}{2}})}{(\frac{d^2y}{d^2x})} \tag{2.9}$$

$$V = (u^2 + v^2 + w^2)^{\frac{1}{2}} \tag{2.10}$$

$$c = \frac{d}{g}\frac{V^2}{r} \tag{2.11}$$

in which r = the radius of the curvature of end depth streamline .

d = the depth of the flow,

c = the pressure head correction.

2. 2.6 Determination of momentum coefficient

In the previous EDR investigations, most of the studies employed the momentum equation that excluded data obtained for the end depth momentum coefficient β near the free overfall. Thus.

$$\beta = \frac{\int u^2 dA}{V^2 A} \tag{2.12}$$

V = mean velocity u = velocity at various y locations

For approximate values, energy coefficient α and momentum coefficient β can be computed by the following formulas:

$$\beta = 1 + \varepsilon^2 \tag{2.13}$$

Where $\varepsilon = \frac{v_m}{V} - 1$

v_m = the maximum velocity

V = mean velocity

On the basis of the extrapolated three components velocity data near the end section, the momentum coefficient β can be determined using the above equation.

2. 2.7 Energy relations

The governing equation used for the energy analysis is the Bernoulli Equation. The total energy E can be expressed as follows:

$$E = Z_1 + \frac{p_1}{\gamma} + \frac{V_1^2}{2g} = Z_2 + \frac{p_2}{\gamma} + \frac{V_2^2}{2g} = const \qquad (2.14)$$

in which $V = \sqrt{u^2 + v^2 + w^2}$

$Z + \frac{p}{\gamma}$ =static pressure head

$\frac{V^2}{2g}$ = total velocity head

Outside the maximum velocity point, near the end depth, the total energy at different sections is determined. To this end, static pressure pitot tube is used to find the static pressure head. The LDA gives the three velocity components. The energy relationships are determined by using the velocity and static pressure head field data to confirm the

fact that in the region above the maximum velocity point (outside of the boundary layer), the total energy E is essentially constant in the flow field near the end depth.

2.2.8 Relations for the end depth and channel discharge

Past theoretical and experimental investigations have shown that a relationship exists between the flow rate and the depth at the free overfall of a channel. Such a relationship enables, in principle, the use of the free overfall as a discharge measuring structure.

Eq.2.15 is the relation between the discharge and the critical depth.

$$Q^2 = gA_c^3 / B_c \tag{2.15}$$

In which A = cross-sectional area;

B_c = the surface width.

According to Eq.2.3a, Eq.2.3b and Eq.2.15, Eq.2.3 may be arranged to the form

$$A_c / B_c(\beta A_c^2 / A_c - A_c) = A_c Y_{gc} - KA_c Y_{gc} \tag{2.16}$$

from trapezoidal channel dimension analysis

$$Y_g = \frac{(3+2X)\cdot y}{6(1+X)} \tag{2.16a}$$

$$\frac{A}{B} = \frac{(1+X)\cdot y}{(1+2X)} \tag{2.16b}$$

In which $X = \frac{My}{b}$, M =side slope, b =the base width. K = pressure coefficient

Substitution of Eq.2.16a and Eq.2.16b with appropriate subscripts into Eq.2.16:

$$\left\{\frac{(3+2X_c)\cdot(1+2X_c)}{6\cdot(1+X_c)^2} - K\cdot\frac{(1+2X_c)\cdot X_c^2(3+2X_c)}{6\cdot(1+X_c)^2}\right\} = \beta\cdot\frac{\left(X_c(1+Xc)\right)}{X_c(1+Xe)} - 1 \tag{2.17}$$

and then simplify it:

$$A_1 - K \cdot A_2 B_1 = \beta \frac{A_3}{B_2} - 1 \qquad (2.18)$$

in which

$$A_1 = \frac{(3 + 2X_c) \cdot (1 + 2X_c)}{6 \cdot (1 + X_c)^2}$$

$$A_2 = \frac{(1 + 2X_c)}{6 \cdot (1 + X_c)^2}$$

$$A_3 = X_c (1 + Xc)$$

$$B_1 = X_c^2 (3 + 2X_c)$$

$$B_2 = X_c (1 + Xe)$$

Eq.2.18 sets the relationship between end depth and critical depth. and from equation 2.15 we can get discharge Q.

2.3 Equipment and procedure

2.3.1 Equipment

Tests were conducted in a smooth stainless steel channel having a polished surface (Fig 2.5). In order to get some useful experimental data, suitable dimensions are determined for the flume; the horizontal channel is made of stainless steel. A side slope 1:1, a base width 0.127m and a height of 0.334 is selected, thereby ensuring a sufficiently large end depth for variously accurate measurements. The length of the flume is 6.85m, at the end

section 0.70m Plexiglas is used to facilitate the measurement by Laser-Doppler-Anemometer (LDA) and at the connection between the rectangular inlet tank and trapezoidal flume, a warped transition 3m long connected the head box of rectangular cross-section to the test channel to reduce flow turbulence. Additional baffles and honey-comb sections and screens in the head box were set in the head box to provide low turbulence flow in the channel.

The discharge was measured using a standard 30-degree V-notch. The maximum error in the discharge measurement by the standard 30^0 V-notch is estimated to be 3%. The water profile was measured by point gage and the static pressure was measured by a screwdriver type pitot tube directly above the flume.

Depth measurement was done with a point gage, which had a resolution of 0.1mm. Wall and static pressure head measurements were made using an inclined monometer capable of reading to the nearly 0.2mm. A second vertical probe was used to measure the pressure head at different locations A, B, C and D of the end section (Fig 2.3).

2.3.1.1 Laser-Doppler-Anemometer (LDA) probe setup

A Dantec Laser-Doppler-Anemometer (LDA) is used to find velocity components. In position 1 (Fig.2.3 and Fig.2.6), one can measure the u and w components through the channel bottom. In position 2 (Fig.2.3 and Fig.2.6), one can find the axial velocity u and the vertical velocity component v at any point, where the lateral velocity component w is determined earlier. The maximum error in the velocity measurement is estimated to be 1%. The probe can be moved in steps of 0.06mm in the directions of x, y and z (Fig.2.6).

Velocity data at the end depth is obtained by extrapolating the velocity data collected in the region upstream and downstream of the end depth section.

2.3.1.2 Laser-Doppler-Anemometer (LDA)

A Dantec two-dimensional LDA unit equipped with a two-dimensional fiber-optic probe was used to obtain the velocity surveys. The laser power was 300mw. Its measuring volume had a radius of 0.078 mm wide and a length of 0.66 mm. The light scattered in the measuring volume was collected by photo multipliers and processed to get the flow velocity. The maximum error in the velocity measurement was estimated to be 1%. The fiber-optic probe was positioned with the help of an automatic traverse, which could move in the x, y and z directions (Fig 2.6) and provide a resolution of 0.0025mm.

2.3.2 Experimental procedures:

2.3.2.1 End depth (y_e) and flow profile measurement:

The end depth and flow profile are measured by a metric point gage to the measure 0.1mm.

2.3.2.2 Velocity Measurement by LDA

To determine u, v and w, the laser unit is used. Due to the limitations of the LDA device, the velocities could not be measured accurately at the end section. To measure the velocities with the laser, one must keep the laser beams passing through a flat surface. In

order to get the velocity at the end section, several locations y=0, x=1.5, 6.0, 12.0 cm which are shown in Fig.2.7 are selected and the velocities are measured. After that, the extrapolation technique is introduced to get the end depth velocity. To get the vertical velocity along the flume, the position 2 (Fig.2.3 and Fig.2.6) was used for the LDA system. A grid was used to get the vertical component near the end section.

2.4 Discussion of results

2.4.1 Static pressure head data for end depth

As flow approaches a free overfall, the mean velocity increases considerably and imparts a strong vertical curvature to the flow profile. Consequently, the pressure distribution at the end section is nonhydrostatic. The pressure at the upper and the lower nappe is zero. Within the flow near the end section was measured to be greater that zero. Table 2.1 shows the pressure distribution along the four different sections near the end depth, which was determined by the static pitot tube. Fig.2.8 to Fig.2.12 separately illustrate the pressure distribution in a trapezoidal channel at the brink sections.

The end depth pressure coefficient, k, was firstly determined by Replogle (1962) both for triangular and rectangular channels. According to him, for the rectangular and triangular channel, the pressure coefficient is:

k_t=0.175

k_r =0.215

Then pressure coefficient K value defined earlier (1.1) for trapezoidal channel in present test after weighted calculating is:

K=0.269

Delleur(1956),after a systematic theoretical analysis supplemented by tests, suggested the following K values

$$-5 < \frac{S_0}{S_c} < 1 \qquad K = 0.30 + \frac{\sqrt{1 - \frac{S_0}{S_c}}}{8}$$

Here, S_0 = the bed slope and S_c is the critical slope.

In the closure of Diskin's paper (1961), Replogle's value k and Deller's K value was compared as follow:

$$K = \frac{4}{3}k$$

As mentioned before, Keller and Fong (1989) got a pressure coefficient for trapezoidal channel through a combination of the rectangular and the triangular sections and involving a nonzero pressure distribution at the brink section, based on measurements of Replogle (1962).

Keller's end depth pressure coefficient governing equation is given below:

$$K = \frac{4}{3}k = \frac{4 \cdot (0.125 + 0.175X_e)}{3 \cdot (1 + 0.175X_e)}$$

$$X_e = \frac{My_e}{b}$$

2.4.2 Energy coefficient α and momentum coefficient β

It must be added that Replogle (1962) provided the values of α and β for the rectangular channel near the end depth. According to him:

$\alpha_c = 1.026$
$\beta_c = 1.011$

For the present test (Table 2.2) in a trapezoidal channel:

$\alpha_c = 1.025$

$\beta_c = 1.015$

2.4.3 Streamline pattern and end depth theoretical pressure head

Fig 2.4 shows the six streamlines determined for a channel discharge Q =19.46*l/s*. the bounding streamlines were obtained from the water profile measurement data near the end depth section. Streamlines 2,3. 4 and 5 (Fig.2.4) are evaluated using the velocity profile data at sections H, I and J (Fig.2.4). Since section H is 15 mm away from the brink, the streamline pattern was extrapolated to the brink location where $x = 0$. In Fig.2.4, the pressure head profile measured at location A of the end depth section for Q =19.46*l/s* is compared with the predicted pressure head profile obtained by applying the curvature correction to the hydrostatic pressure head as described in a previous section. The pressure head measured by static pressure probe was accurate and repeated tests yielded nearly identical static pressure data. However, as the correction for pressure distribution varies with the square of the velocity, the errors in the velocity measurement

will appear exaggerated in the predicted pressure data. The close agreement of the measured and predicted pressure at 3 of the 4 locations may be fortuitous.

Measurement of the velocity at different sections15mm, 60mm, and 120mm (Fig 2.4) ahead of the end depth was made out by the LDA in a trapezoidal channel.

Results of all experiments and subsequent analysis are listed in Table 2.3, Table 2.4,and Table 2.5. In all these tables, column2 is the flow axial velocity, column 3 is the ψ value difference, and column 4 is the ψ value at the point. Table 4.6 shows the ψ value of different streamline at different sections.

For the streamlines bounding the upper and lower nappes, additional profile data were obtained in the region beyond the end section to determine the radius of streamline curvature most accurately.

2.4.4 Energy relations

Data related to the three dimension velocity components and the corresponding static pressure head were carried out for three different sections (15mm, 30mm, 60mm near the end depth) and the depth range from 1.5mm to 70 mm. The three dimension velocities were measured by LDA and the static pressure were determined by static pitot tube.

Results of all the experiments and of subsequent analysis are list in Table 2.7, Table 2.8 and Table 2.9. In those tables, columns 2 and 3 list the velocities measured from position

1 and column 4 lists the velocity obtained from position 2 (Fig.2.3 and Fig.2.6). Column 6 lists the static pressure gotten from the static pitot tube, and column 7 is the total energy Column 8 lists the difference ratio between different point total energy and the maximum velocity total energy.

As expected, it appears that the total energy in the region outside the maximum velocity point is nearly constant near the end depth.

2.4.5 Discharge predication by using measured momentum and pressure coefficient near the end depth

Results of all present end depth experiments in the flow rate ranging from 6.24l/s to 21.35l/s and subsequent analysis using the pressure coefficient K, and momentum coefficient β, are listed in Table 2.10 and shown in Fig.2.14, columns 1 and 2 list the measured end depth and discharge values. Column 3 lists the theoretical discharge as predicted from Eq.2.3 with measured β & K value. Columns 4, 5, 6 and 7 list the percent deviation under different condition between the theoretical and experimental discharge values.

Table 2.10 indicates that 66.7 percent of the predictions are within ± 2 percent of the measured flow and 100 percent are within ± 5 percent. These results indicate a very good agreement between experimental and theoretical data.

Column 4 shows the computed values of discharge using both pressure coefficient K, and momentum coefficient β. These predicted results show that for a large portion of the data, the deviation is less than 5% from the measured discharge.

Comparison of the theoretical and experimental discharge values with K without β value (column 5) indicated that 53 percent of the predictions are within ± 2 percent measured flow and 93.3 percent are within ± 5 percent.

In column 6, Comparison of the predicted and experimental discharge values with β without K, the values in the column are better than theoretical discharge without β & K, but the deviation is still too big. From the above analysis, we can see that in the prediction of discharge near the end depth, the pressure coefficient, K, is the dominant factor.

Table 2.11, Table 2.12, Table 2.13, Table 2.14 and Fig.2.15, Fig.2.16, Fig.2.17, Fig.2.18 indicates that the result of Rajaratnam (1970), Keller (1986), Diskin (1961) and Pagliara (1993) shows that the inclusion of β & K improve the dependence of the discharge rate Q on the end depth y_e.

Chapter 3

Rectangular weir flow

This chapter deals with the study of the rectangular weir flow and the application of the hydraulic principle of images to form multislit weirs based on slit weirs.

3.1 Theoretical consideration

The discharge rate Q through a multislit weir (Fig.3.1, Fig.3.2) is a function of the weir width (b), channel width (B), the weir crest height above the channel floor (P), and the driving head (h). The other factors that influence C_d are the density (ρ), the dynamic viscosity (μ), and the surface tension (σ) of the fluid and the gravitational acceleration (g).

$$Q = f_1(b , B , P , h , \gamma , \rho , \mu , \text{n}, \sigma) \tag{3.1}$$

For the multislit unit, the weir discharge coefficient C_d can be expressed in a dimensionless form relating the other parameters as follows:

$$\frac{Q}{bh\sqrt{gh}} = f_2(\frac{nb}{B}, \frac{nb}{h}, \frac{h}{P}, R, W, n) \tag{3.2}$$

$$C_d = f_2(\frac{nb}{B}, \frac{nb}{h}, \frac{h}{P}, R, W, n) * \sqrt{g} \tag{3.2a}$$

$$C_d = bh^{3/2} / Q \tag{3.2b}$$

Here, R is Reynolds number $R = \frac{Q\rho}{h\upsilon}$

W is Weber number $W = \frac{Q^2\rho}{\sigma bh^2}$ and C_d = discharge coefficient

The first three independent ratios in Eq.3.2 are the geometry of the flow boundaries. Eq.3.2b is used as the basic discharge equation in this study. The above discharge equation for a weir cannot be derived exactly since the flow, which is affected by viscosity, surface tension, geometry, geometry ratio of the weir and several other parameters, is very complicated. Therefore, weir types and dimensions are standardized and accurate discharge formulas are developed empirically using extensive experimental data.

3.1.1 Significance of the Geometric Ratios

One of the most significant ratios in Eq.3.2 is (nb)/B. It is a measure of the channel-width-contraction characteristic of the weir. In combination with h/P, it is also an area – contraction ratio. The influence of b/B is similar to that of the corresponding width or diameter ratios, which are used to describe the geometry of orifices. In the present studies, this ratio is taken as (nb)/B, where n is number of active slits. The b/h ratio can be described as a shape parameter. The independent influence of this ratio is believed to be negligible over the full practical range of the other variables. An earlier experiment at Georgia Institute of Technology supports this result. The fact that most of the published conclusions of research on single weirs ignore the b/h ratio indicates that its influence is not evident from the experiment data.

The h/P ratio is a measure of the depth-contraction characteristic of the weir. It is complementary to (nb)/B as an area-contraction ratio. Its influence is said to be represented by the effect of the velocity -of-approach in several published formulas.

3.1.2 The influence of Viscosity

One of the effects of viscosity, which can be ignored in many accelerated fluid motions, is the energy loss, which results from fluid shear. The total loss of energy between the section of head measurement and the crest of a weir is insignificant.

A separation zone occupied by a large eddy occurs in the corner between the weir plate and the bottom of the approach channel. The effect of this occurrence on a low weir, in comparison with the flow pattern for the same weir, is similar to the effect of having a sloping plate upstream of the weir.

A separation zone also occurs in the corner between the side of a slit weir plate and the walls of the approach channel. The effect of this occurrence, in comparison with potential motion, is to reduce the width contraction of the weir nappe. However, no separation zone occurs between the slit weirs.

Viscous shear causes the flow to be retarded in the vicinity of the boundaries. A boundary layer is also formed on the bottom and sidewalls of the approach channel.

3.2 Experimental set-up

Most of the experiments were conducted in a rectangular, horizontal glass flume 60 cm wide, 120 cm deep and 6.85 m long (Fig 3.4), termed as channel 1. There is no need for

ventilating the nappe. since air has access all around the nappe for the weir widths considered. To reduce the turbulence in the channel flow approaching the weirs, a number of screens and honeycombs were installed in the head box attached to the flume. A few experiments related to a single slit weir (b = 36 mm, p =38mm and 80mm) were conducted in a rectangular, horizontal glass flume that is 300 mm wide. 400 mm high and 7 m long (Fig.3.5). It is termed as channel 2.

The multislit weirs are fabricated from 1/8-inch thick stainless steel plates. The beveled weir edges were 1 mm wide (Fig3.1). Three different multislit weir units (n = 3. 7and 15) were tested in the 1 m wide flume. The weir units had weir blocking cover plates that enabled one to convert a 15-unit weir to a seven slit or to a three slit or even a single slit weir unit. This yielded different b/B ratios from a single multislit unit while holding b constant. The number of active slit weirs through which flow passes is denoted as n and the total number of slit weirs including blocked weirs is denoted as N.

A point gauge capable of reading to the nearest 0.1 mm at a location determines the head over the weir 2 m upstream of the weir units in channel 1 and 1.2 m upstream in channel 2. The discharge over the weir is measured using a standard 30^0 V-notch in channel 1 and a 60^0 V-notch in channel 2. The head over the V-notch is always in excess of 80 mm to eliminate the surface tension effects. For very low flows, discharge was measured by weighing the volume of flow collected for 100 seconds or more. The error of discharge measurement is estimated to be3 %.

3.3 Discussion of Results

3.3.1 Variation of C_d with R_e and W_e

The experimental discharge coefficient C_d obtained from equation 3.2b for multislit weirs is shown in Fig.3.6 as a function of the Reynolds number R_e. The best-fit curve for this data is also shown in the same sketch. This curve is essentially the same as the curve denoted by Eq.1.1 for single slit weir (Aydin 1999). As stated earlier, the weirs on either side of the central weir are considered to be its images. This hypothesis is supported by the fact that best fit curve for the multislit weir data is essentially the same as the best fit curve recommended by Aydin (1999) for the single slit, when nb/B used in place of b/B. The data shows a clear dependence of C_d on R_e. There is a slight scatter of the data that indicates the influence of the other parameter, such as W_e, b/h and h/p. As stated earlier the effect of (nb)/B on C_d is insignificant for the range of (nb)/B chosen. When the effects of viscosity and surface tension are absent, the discharge coefficient tends to reach an asymptotic value of 0.61 (Fig.3.6).

Fig.3.7 shows the variation of discharge coefficient C_d with the Weber number W_e considering all the data. The scatter of the data in this presentation is excessive. Fig.3.8a, to Fig.3.8d present the data of Fig.3.7 by segregating them in terms of different Reynolds number ranges. This presentation underscores the fact that in the range of test variables covered, C_d does not significantly vary with W_e and the large scatter of data in Fig.3.7 should be traced to the variations of Reynolds number in the four different series of tests.

The slight increase in C_d for very low W_e values in Fig.3.8a to Fig.3.8d are to be traced to the corresponding low Reynolds numbers associated with low W_e values. This is true,

since the value of W_e depends on h and R_e depends on $h^{1/2}$ and C_d increases considerately with a decrease in R_e at low R_e values. (Fig.3.6)

3.3.2 Variation of C_d with h/p

Fig.3.9 shows that there is a large scatter in the data when C_d is plotted as a function of h/p. However, when the data for C_d and h/p are segregated by restricting the data to a short range of Reynolds numbers, some order appears to prevail (Fig.3.10 and Fig.3.11). A slightly increase in C_d for very low h/p in each case (Fig.3.10 and Fig.3.11) can be traced to the fact that low h/p denotes low R_e. At low R_e, C_d varies strongly with R_e (Fig.3.6).

Chapter 4

Conclusions and suggestions for future studies

4.1 End depth studies

(1) The static pressure head (p/γ) at the end depth section can be accurately predicted by applying the curvature correction to streamlines.

(2) The pressure head correction is a dominant factor that correctly determines the relation between Q and y_e.

(3) The total energy ($Z+\frac{p}{\gamma}+\frac{V^2}{2g}$) is essentially constant in the region above the maximum velocity point near the end depth.

(4) Using K and β determined during the tests an accurate relationship between Q and y_e can be obtained.

4.2 Multislit weir studies

1.The hypothesis that weirs on either side of the central weir can be considered to be images of the central weir is supported by test data.

2.Multislit can be used to measure a very wide range of discharges. For instance, the multislit weir with N = 15 can measure a wide range of discharge in the range of 40 l/s (n = 7) to 0.7 l/s (n = 1).

3. For the range of weir parameters selected in the present test, C_d mainly varies with R_e.

4.3 Suggestion for the future studies

1. The procedure suggested for improving the accuracy of the relation between the end depth and the channel discharge can be extended to channels that are not horizontal and to channels that are rough.

2. Tests may be preformed to verify the concept of multislit weir to a wilder range of b/B.

References

[1] Ali,K. M. and Sykes, A., "Free vortex theory applied to free overfall." Journal of the Hydraulics Division, ASCE, 98(5), 1972, pp973-979.

[2]. Aydin,I., Ger, A. M. and Hincal, O., "Measurement of Small Discharge in Open Channels by Slit Weir," Journal of Hydraulic Engineering, ASCE, Vol. 128, No. 2, Feb 2002, pp234-237.

[3] Bauer, S. and Graf, W., "Free Overfall as Flow Measuring Device." Journal of Irrigation and Drainage Division, ASCE, Vol. 97, No IR1, March, 1971, pp73-83.

[4] Bos, M. G., *Discharge Measurement Structures*. 3rd Ed., International Institute for Land Reclamation and Improvement/ILRI, Wageningen, The Netherlands, 1989.

[5] Chow V. T., *Open Channel Hydraulics*, McGraw-Hill Inc., New York, 1974.

[6] Delleur, J.W., Dooge, J.C.I., and Gent K.W., "Influence of Slope and Roughness on the Free Overfall." Journal of Hydraulic Engineering, ASCE, Vol.82, No. HY 4, Aug. 1956, pp. 1038-30-1038-35.

[7] Diskin, M.H., "End Depth at a Drop in Trapezoidal Channels." Journal of the Hydraulics Division, ASCE, Vol.87, No. HY 4, July 1961, pp.11-32.

[8] Fathy, A. and Shaarawi, M., "Hydraulics of the Free Overfall." Proceeding, ASCE, Vol. 80, Proceedings –Separate No. 564, Dec 1954, pp. 564-1-564-12.

[9] Gupta, R.D., Jamil,M., and Mohsin, M., "Discharge Prediction in Smoth Trapezoidal Free Overfall." Journal of Irrigation and Drainage Engineering, ASCE, Vol. 119, No.2 1993, pp215-224.

[10] Hager, W.H., "Hydraulics of plane Free Overfall." Journal of Hydraulic Engineering, ASCE, Vol. 109, No.12, Dec., 1983, pp1683-1697.

[11] Hamid, H.I., Discussion of "End Depth at a Drop in Trapezoidal Channels." By M.H. Diskin. Journal of the Hydraulic Division, ASCE, Vol. 88, 1962, pp133-136.

[12]. Han,T.Y. and Chow, W.L., "The Study of Sluice Gates and Sharp-Crested Weirs Through Hodograph Transformations," Journal of Applied Mechanics, ASME, Vol.48,June1981, pp. 229-234.

[13] Keller, R. and Fong, S., "Flow Measurement with Trapezoidal Free Overfall." Journal of Irrigation and Drainage Engineering, ASCE, Vol. 115, No.1 Feb 1993, pp125-136.

[14] Kandaswamy,P.K. and Rouse, H., "Characteristics of Flow Over Terminal Weirs and Sills." Journal of the Hydraulic Division, ASCE, Vol.83, No. HY4, August 1957, pp.1345-1 - 1345-13.

[15] Kindsvater, C. E. and Cater, R.W., "Discharge Characteristics of Rectangular Thin-Plate weirs." Journal of the Hydraulic Division, ASCE, Vol.83, No. HY6, Dec, 1957, pp.1-36.

[16] Litsa Anastasiadou-Partheniou and Evangelos Hatzigiannakis, "General End-Depth-Discharge Relationship at Free Overfall in Trapezoidal Channel." Journal of Irrigation and Drainage Engineering, ASCE, Vol. 121, No.2, March/April, 1995, pp143-151.

[17] Neogy, B., "Brink Depth for Trapezoidal Broad-Crested Weir." Journal of Hydraulic Division, ASCE, Vol. 98, No.HY12, Dec., 1972, pp2171-2189.

[18] Olson, M. G. *Engineering Fluid Mechanics*. 2rd Ed., International Textbook Company, Pennsylvania, 1968.

[19] Ramamurthy, A. S., "Flow over Sharp-Crested Plate Weirs." Journal of Irrigation and Drainage Engineering, ASCE, Vol. 113, No.2, 1987 pp163-172.

[20] Rajaratnam, N. and Muralidhar,D., "End Depth for Circular Channel." Journal of the Hydraulic Division, ASCE, Vol. 90, 1964, pp90-119. (A)

[21] Rajaratnam, N. and Muralidhar,D., "End depth for Exponential Channels." Journal of Irrigation and Drainage Division, ASCE, Vol. 90, No. IR 1 March, 1964, pp17-39. (B)

[22] Rajaratnam, N. and Muralidhar.D., "Characteristics of the Rectangular Free Overfall." Journal of Hydraulic Research, ASCE, Vol. 6, No.3 1968, pp233-258.

[23] Rajaratnam, N., Discussion of "End Depth at a Drop in Trapezoidal Channels." by M.H. Diskin. Journal of Hydraulic Division, ASCE, Vol. 88, 1962, pp119-130.

[24] Rajaratnam, N. and Muralidhar,D., "The Trapezoidal Free Overfall." Journal of Hydraulic Research, Vol. 8,1970 pp419-447.

[25] Rajaratnam, N., Muralidhar,D., and Beltaos, S., "Roughness Effects on Rectangular Overfall." Journal of Hydraulic Division, ASCE, Vol. 102, 1976, pp599-614.

[26] Replgle, J., A, Discussion of "End Depth at a Drop in Trapezoidal Channels." by M.H. Diskin. Journal of the Hydraulic Division, ASCE, Vol. 88, 1962, pp161-165.

[27] Rouse, H., "Dischargement Characteristics of the Free Overfall." Civil Engineering, ASCE, Vol. 6, No.4 April 1936, pp257-260.

[28] Sarginson, E. J., "The Influence of Surface Tension on Weir Flow" Journal of Hydraulic Research, Vol. 10, 1972, pp431-446.

[29]. Subhash C. Jain., *Open - Channel Flow*, JOHN WILEY&SONS Inc., New York, 2000

[30] Terzidis, G., "Hydraulic Characteristics of a Rectangular Free Over-fall." Hydrotechnika, 2nd Panhellenic Conf.E.Y.E. Plesio, Greece, 1985, pp11-28.

[31] Terzidis, G., and Anastasiadou-Patheniou, L., Discuession of "Flow Measurement with Trapezoidal Free Overfall." by Keller, R., and Fong, S., Journal of Irrigation and Drainage Engineering, ASCE, Vol. 116(6), 1990, pp860-862.

[32] Vallentine H.R., *Applied Hydrodynamics*, Butterworths, London, 1967.

Appendix A: Figures

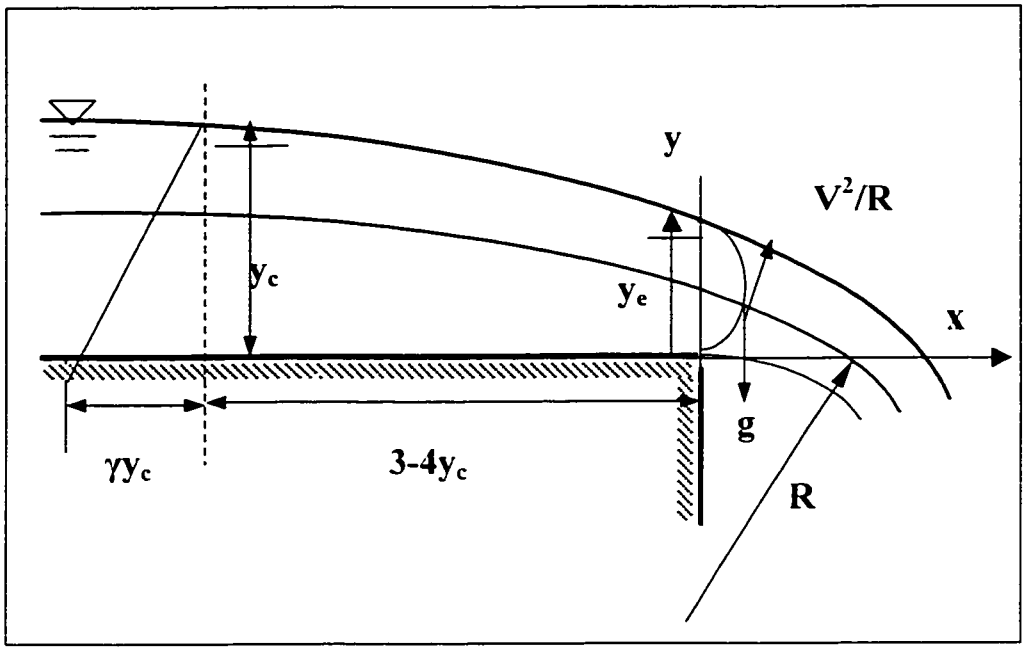

Fig 2.1 Pressure Distribution in Curvilinear Flow

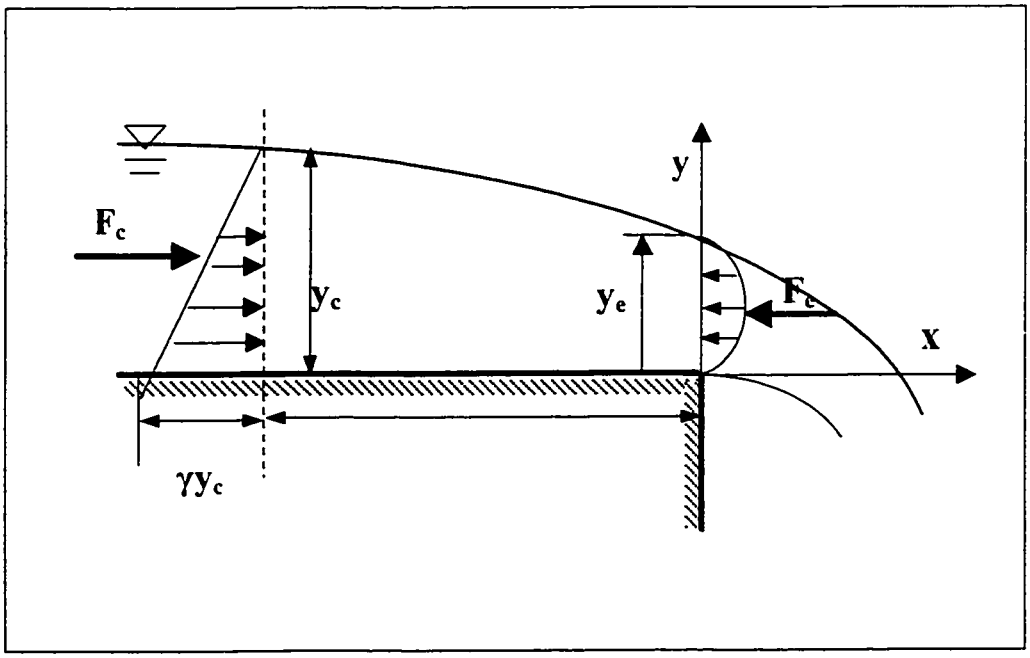

Fig 2.2 Control Volume for Theoretical Analysis

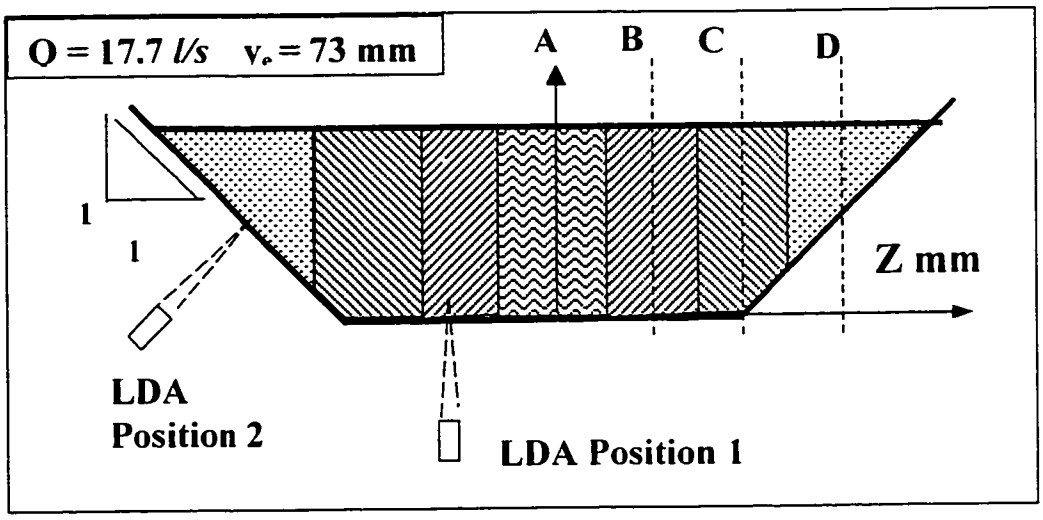

Fig.2.3: End Depth Pressure Head Measurement Sections

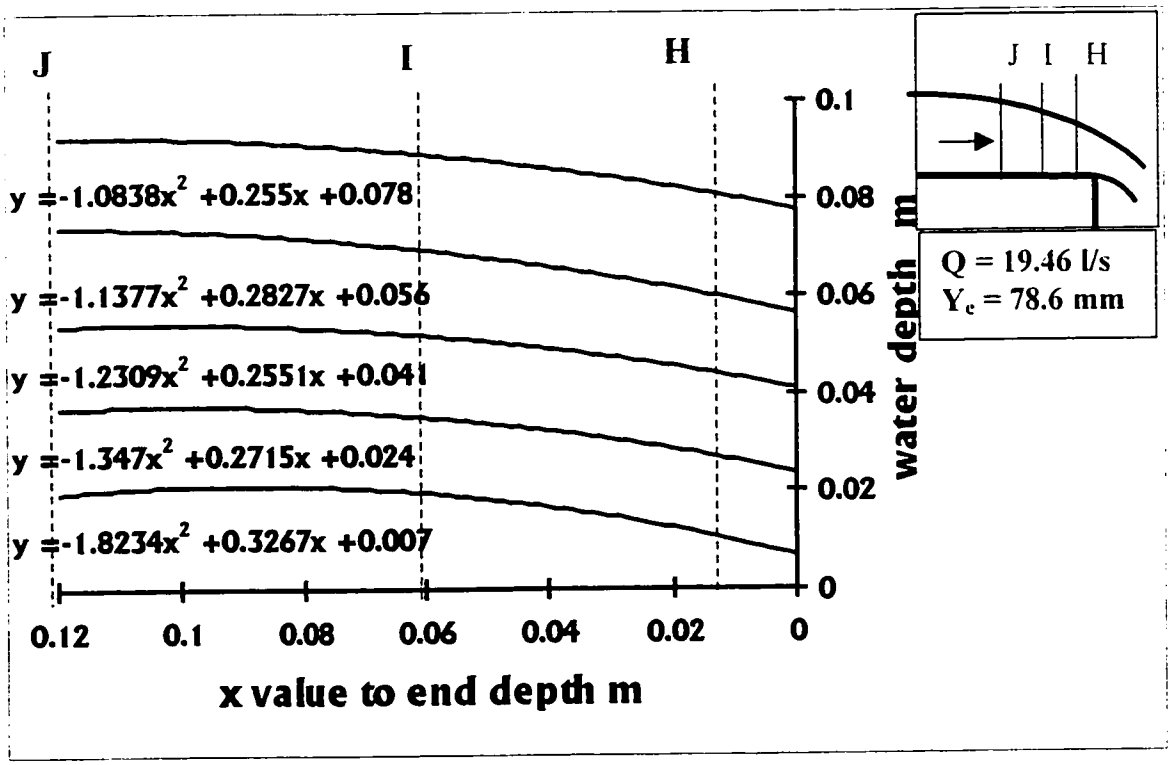

Fig.2.4: Streamlines Near End Section

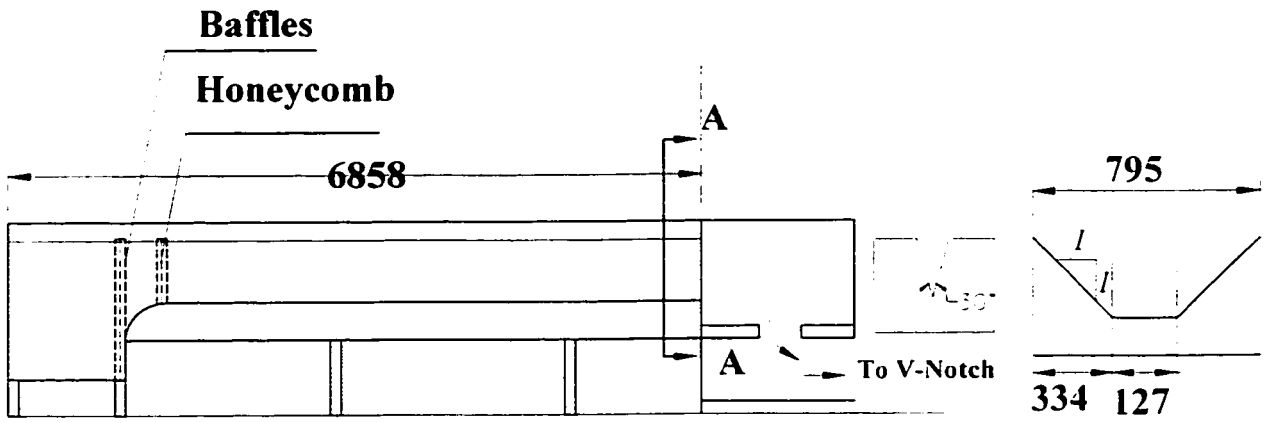

Fig 2.5: Diagram of Trapezoidal Channel

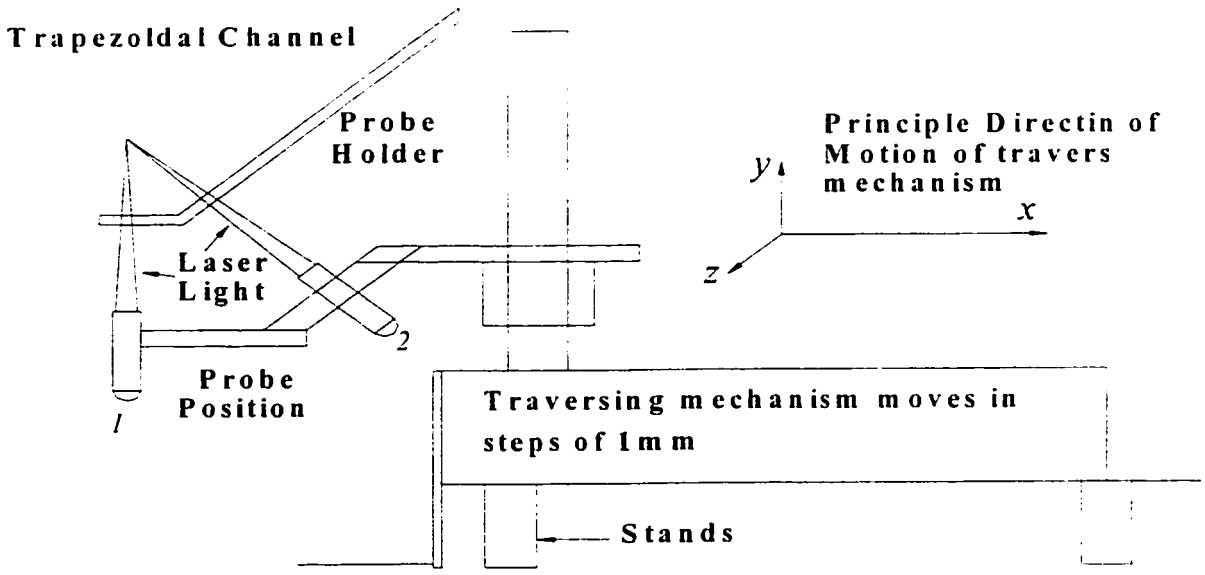

Fig 2.6: Probe Holder

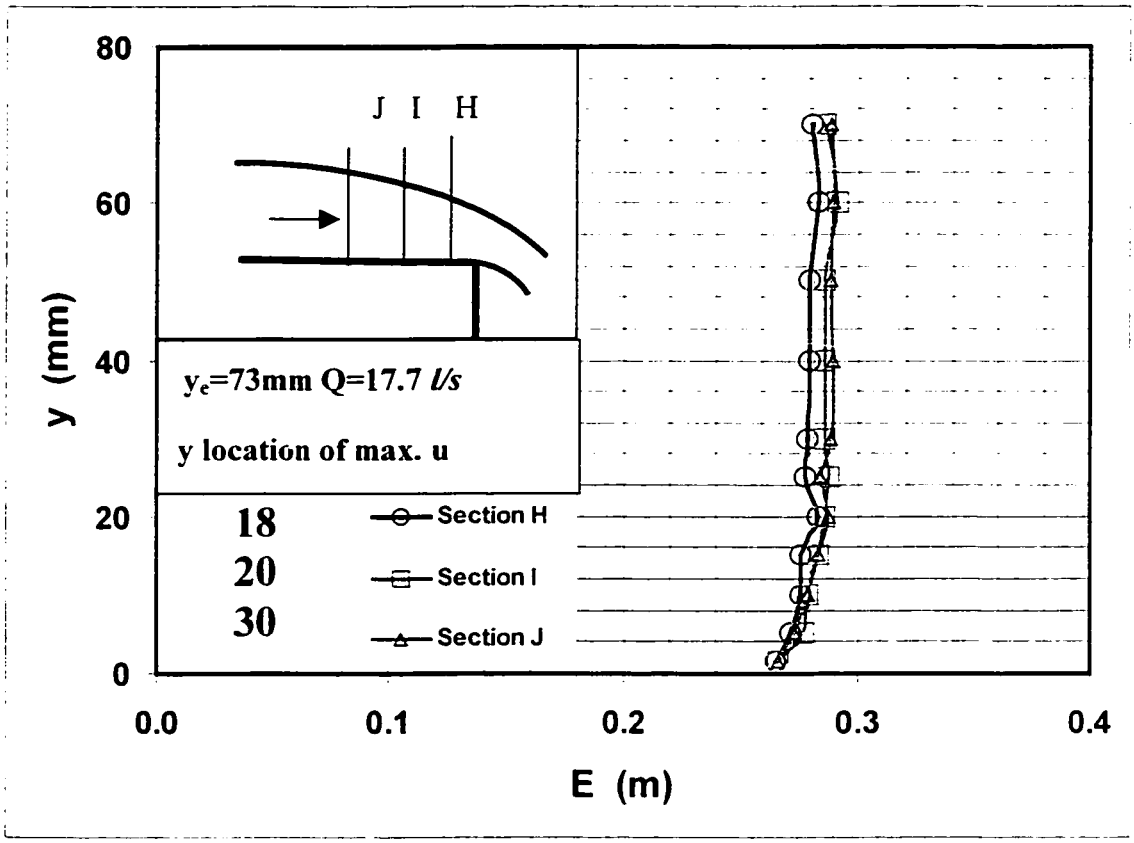

Fig 2.7 Verification of Total Energy at Section E, F, G Profile

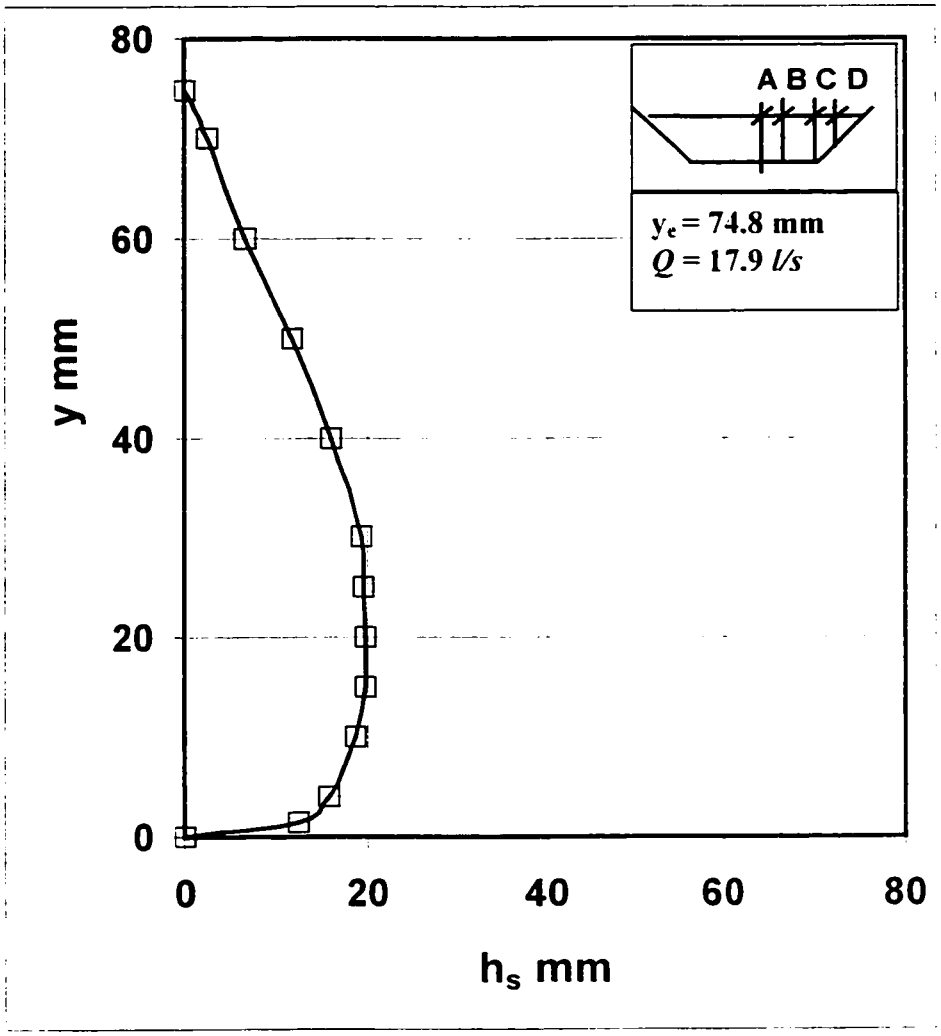

Fig 2.8 Pressure Head Distribution at Section A

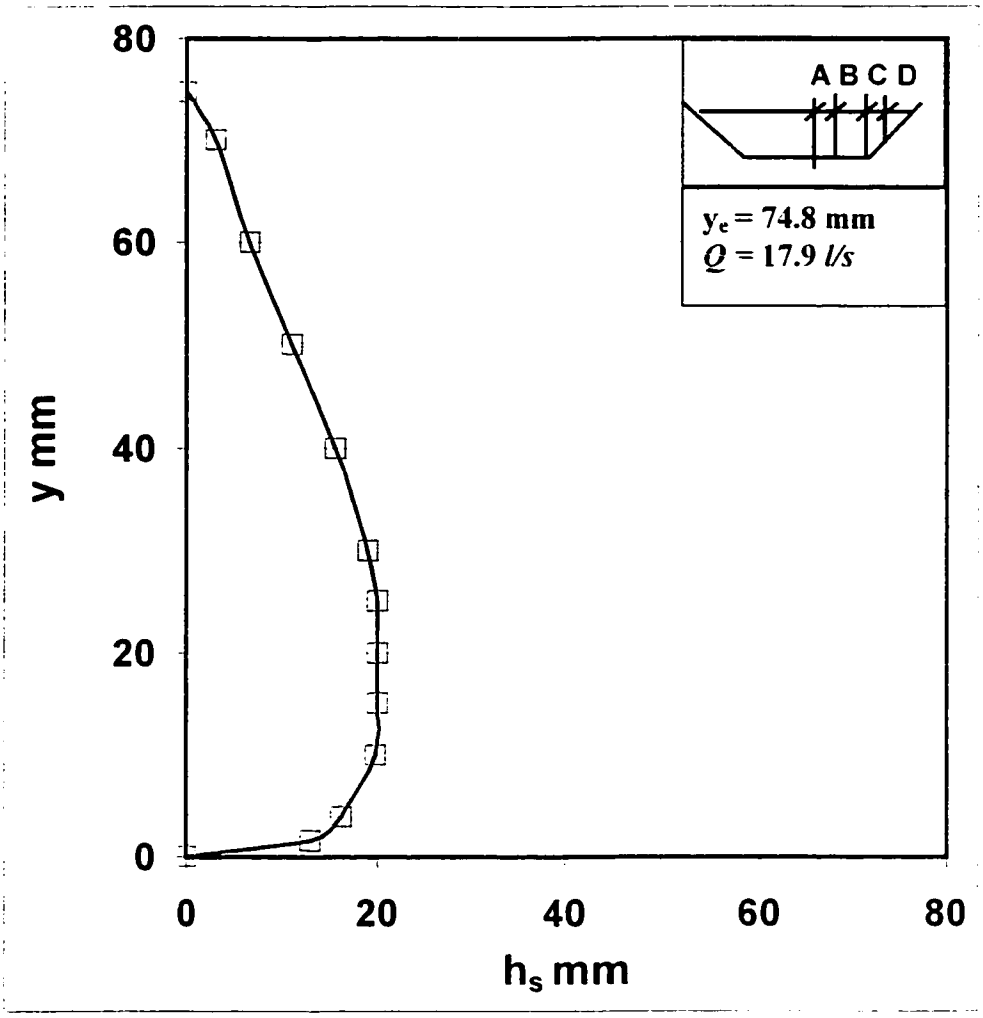

Fig 2.9 Pressure Head Distribution at Section B

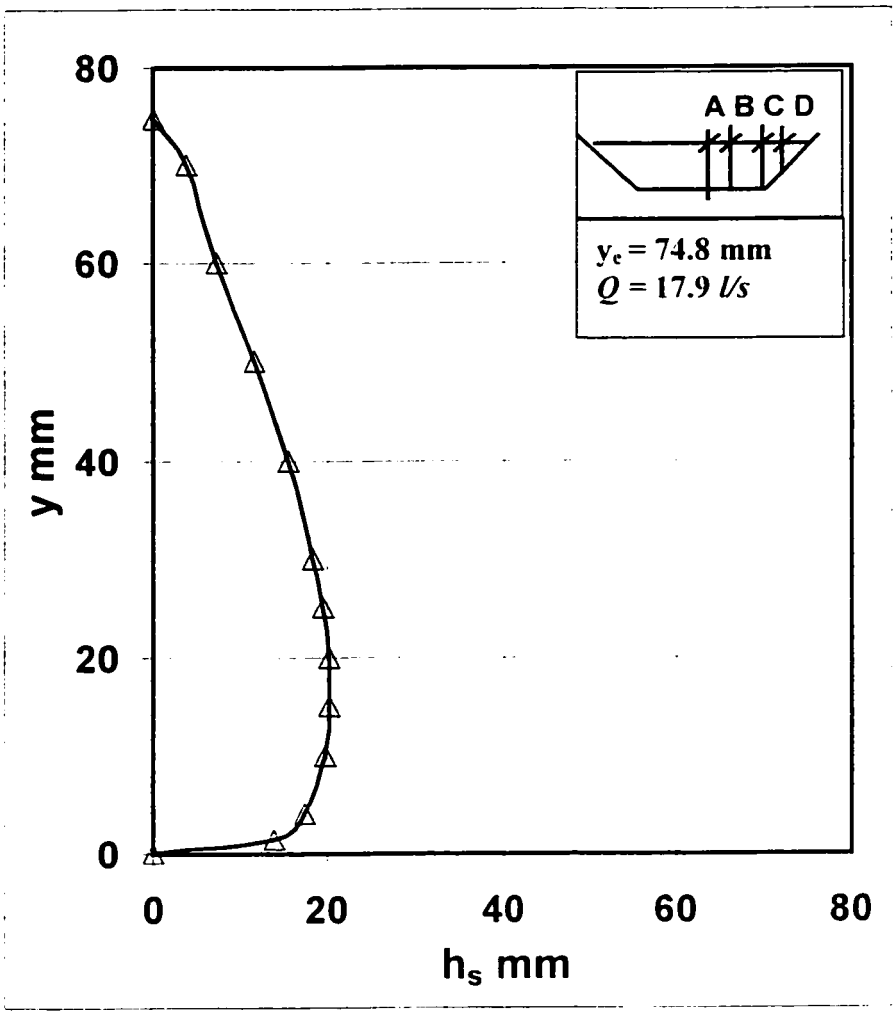

Fig 2.10 Pressure Head Distribution at Section C

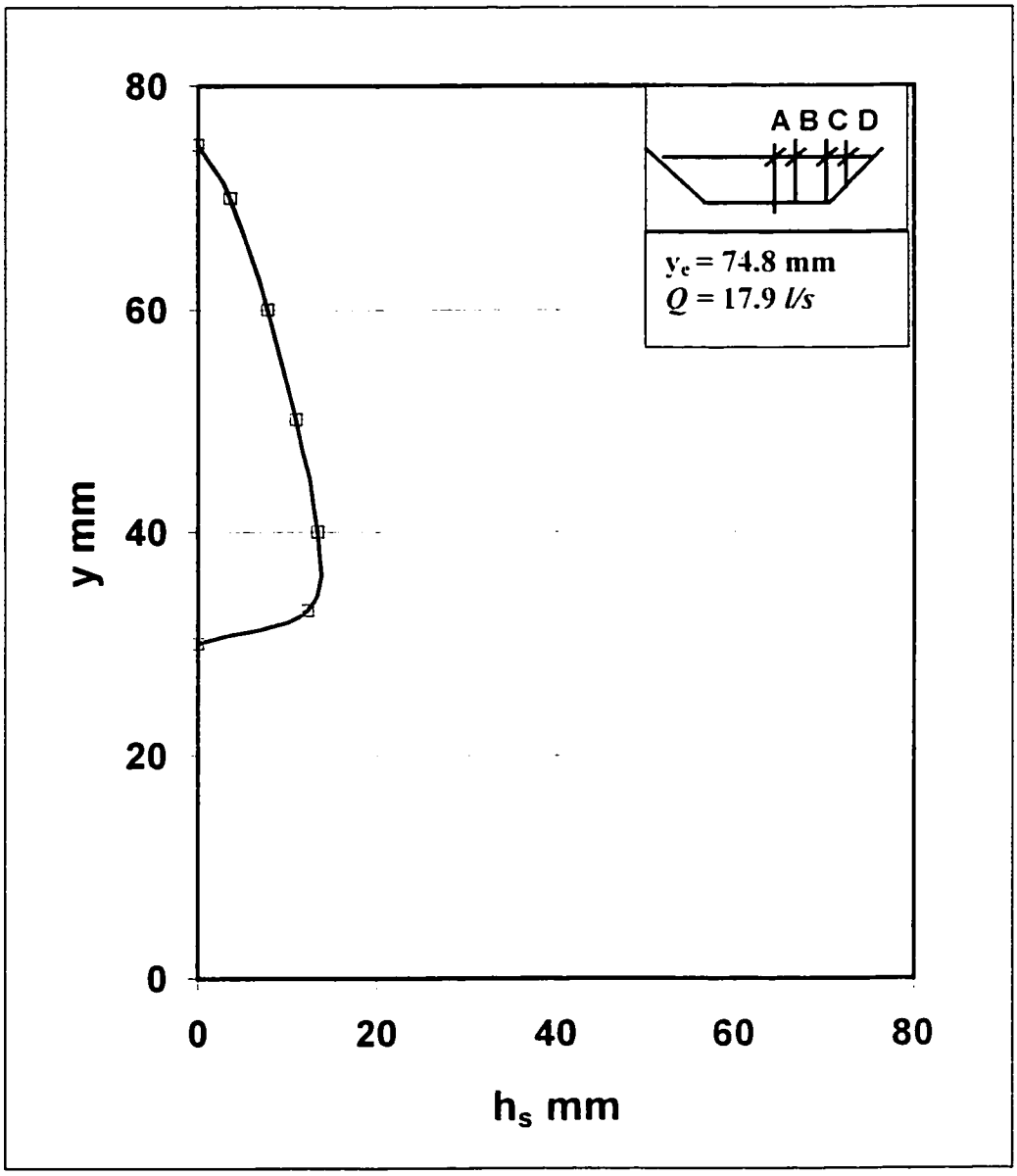

Fig 2.11 Pressure Head Distribution at Section D

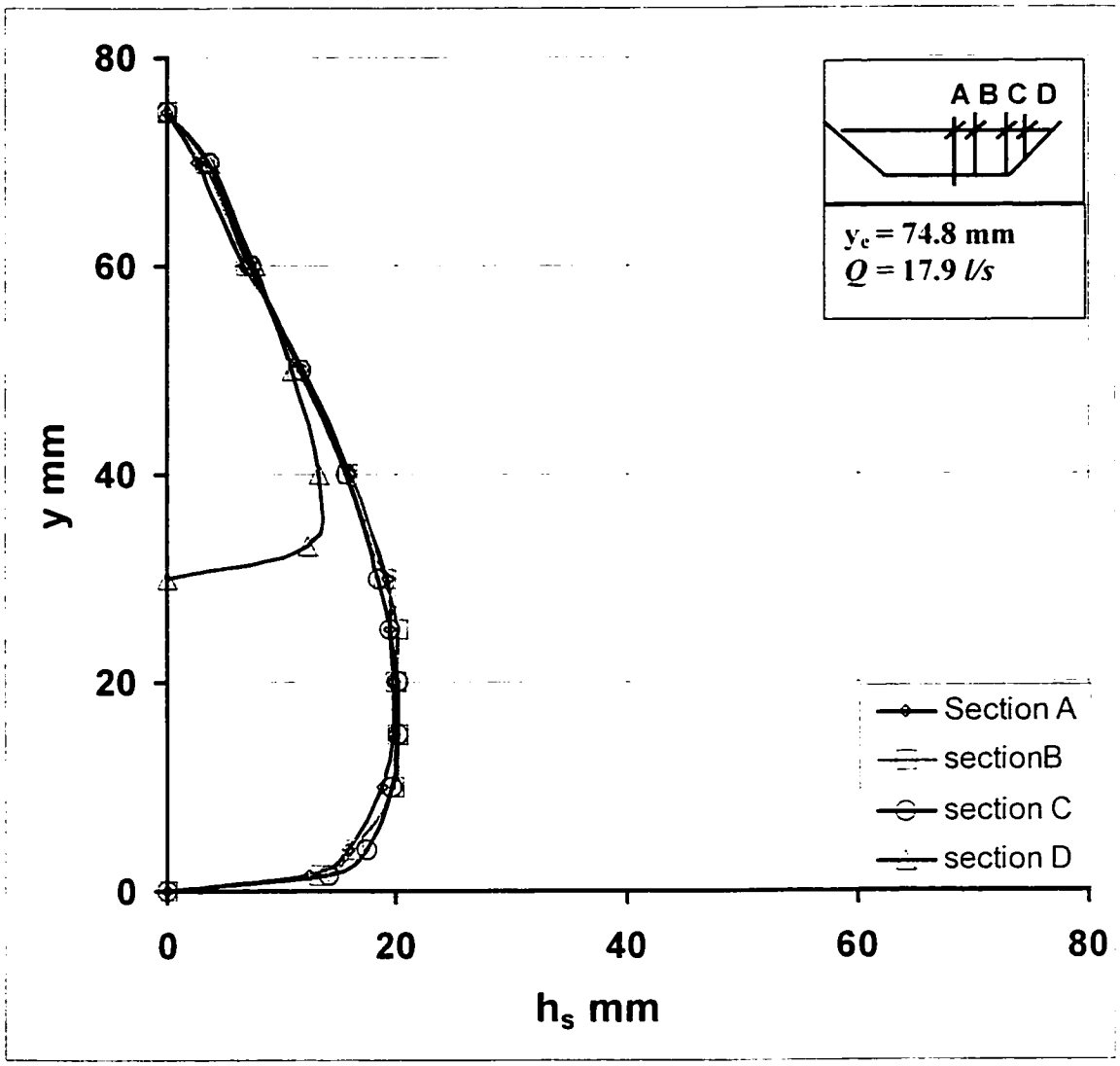

Fig 2.12 Pressure Head Distribution at Section A.B.C.D

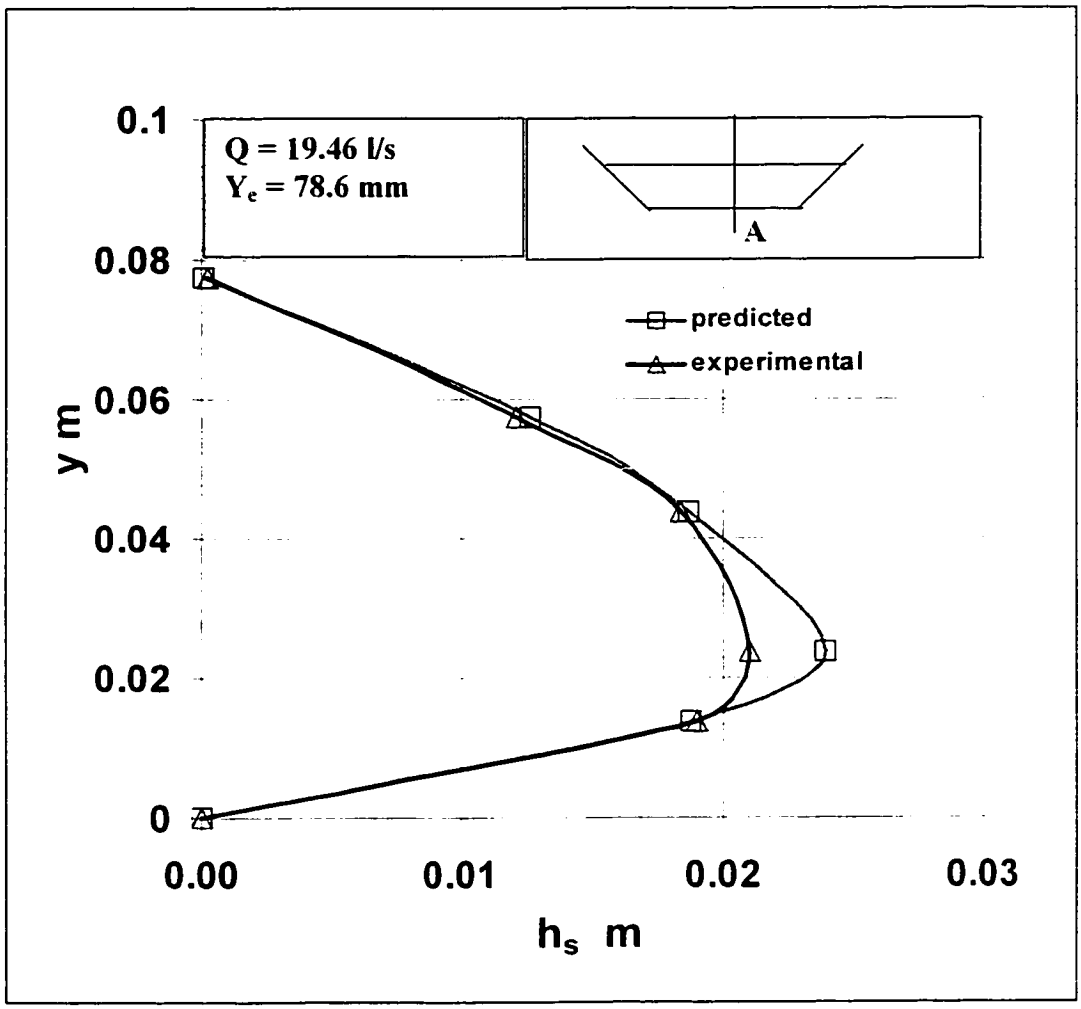

Fig 2.13 End Depth Theoretical and Experimental Pressure Head Profile

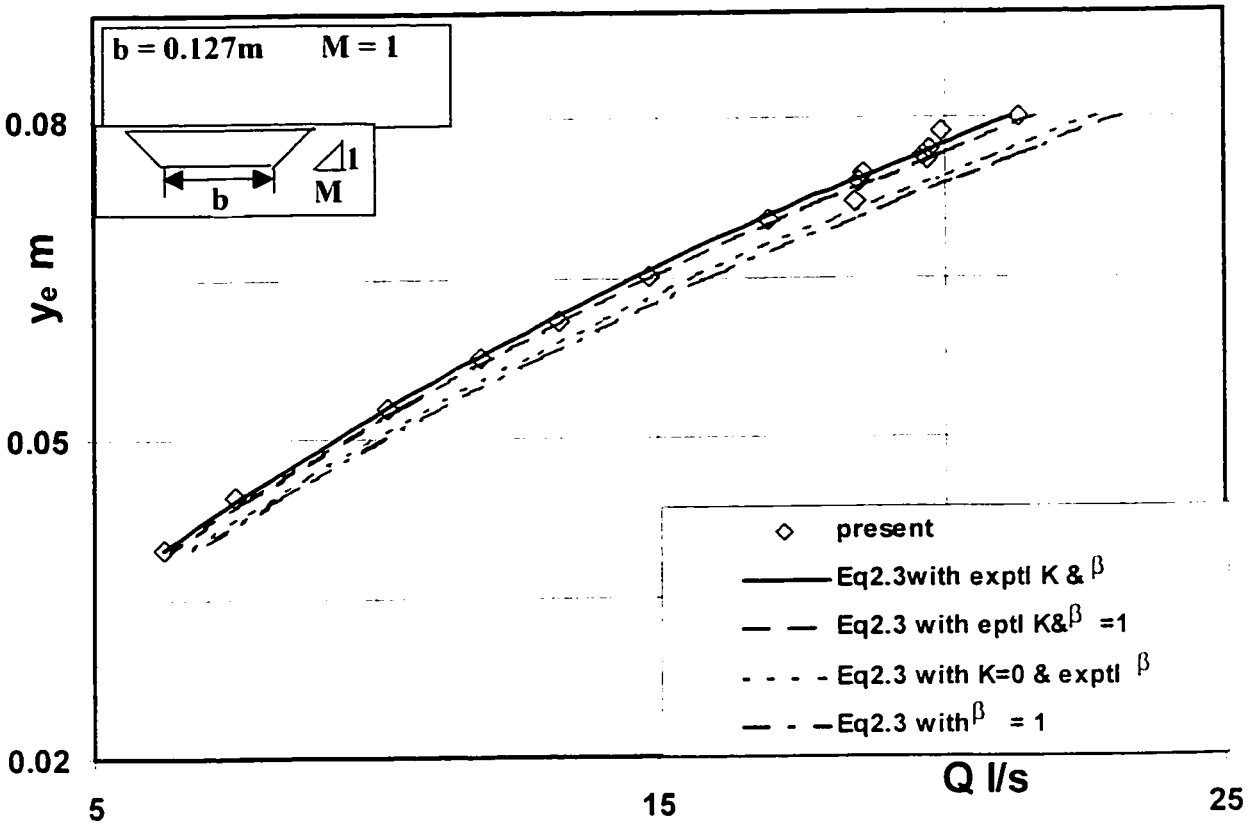

Fig 2.14 Discharge versus End Depth [(Chaozhai 2002) Experiment]

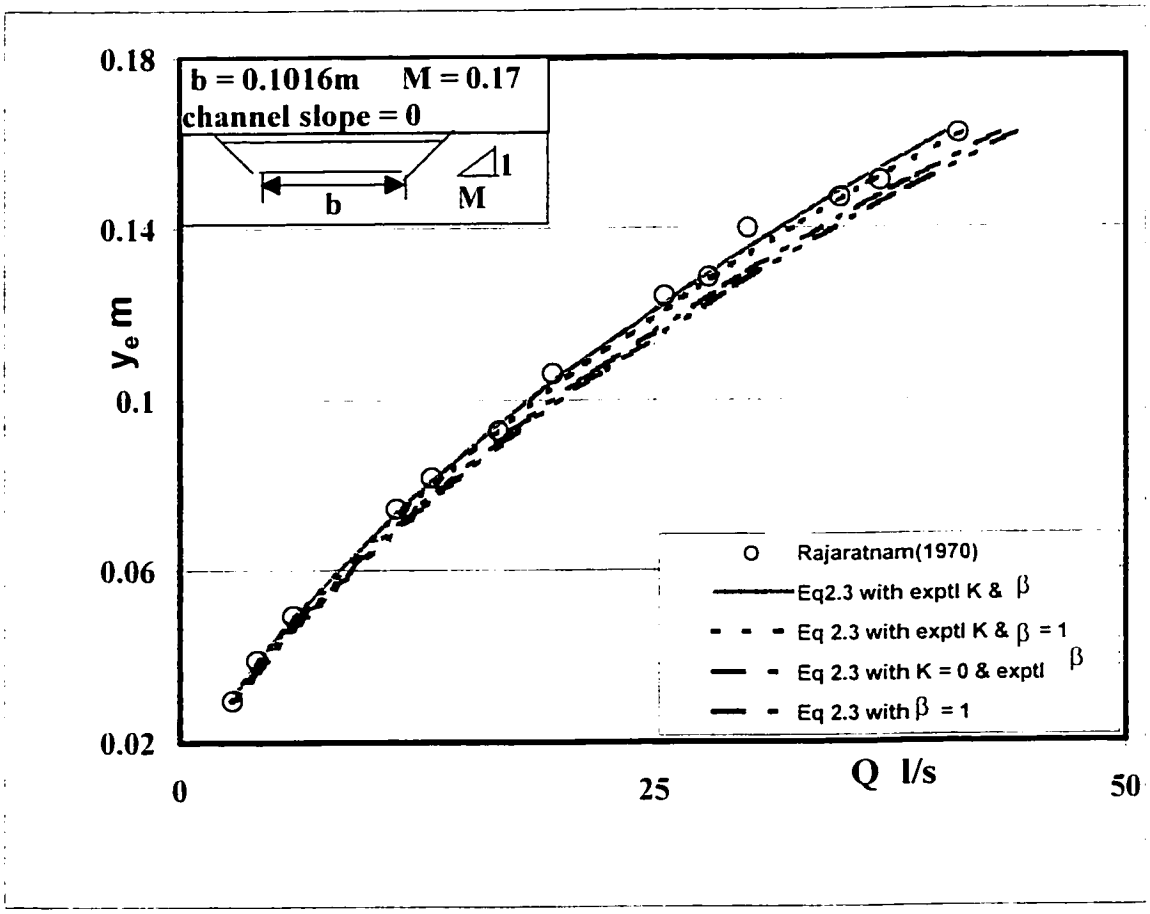

Fig 2.15 Discharge versus End Depth [(Rajaratnam 1970) Experiment]

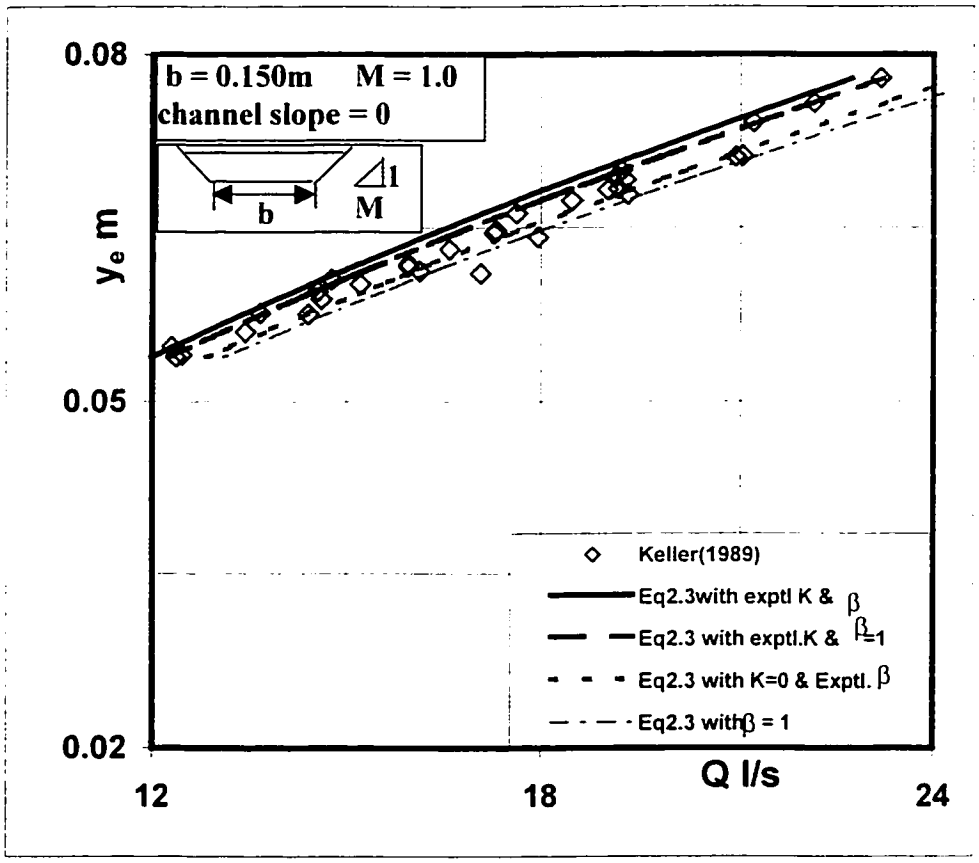

Fig 2.16 Discharge versus End Depth [(Keller 1989) Experiment]

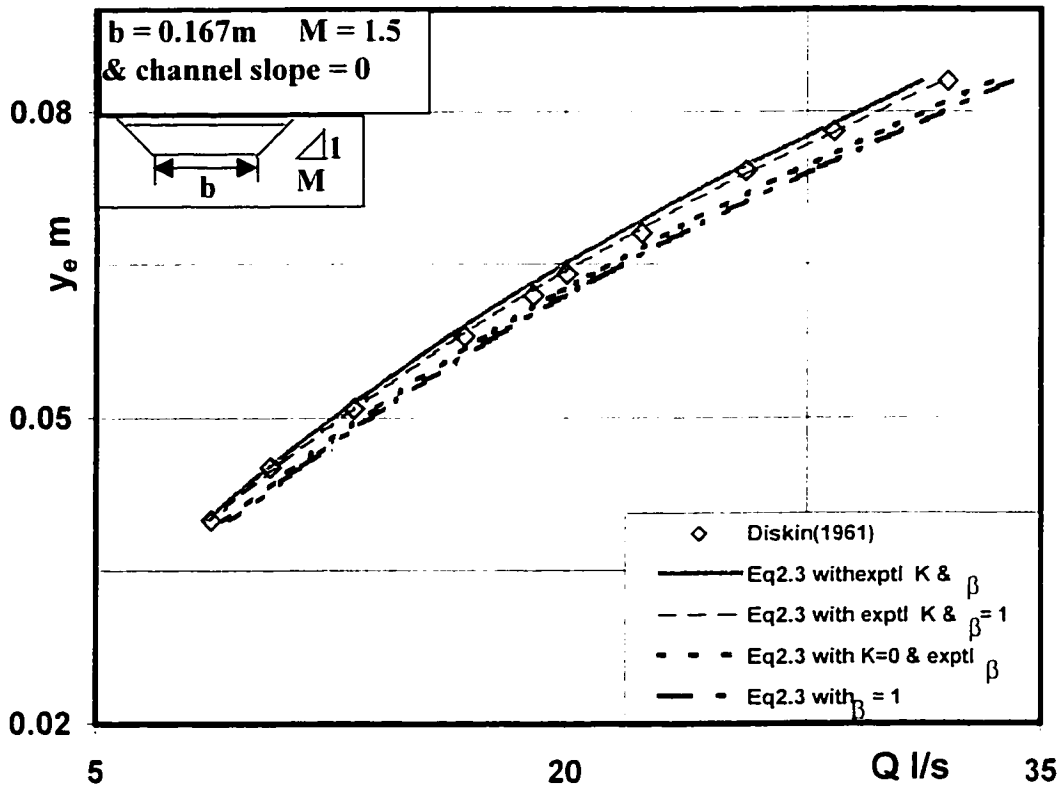

Fig 2.17 Discharge versus End Depth [(Diskin 1961) Experiment]

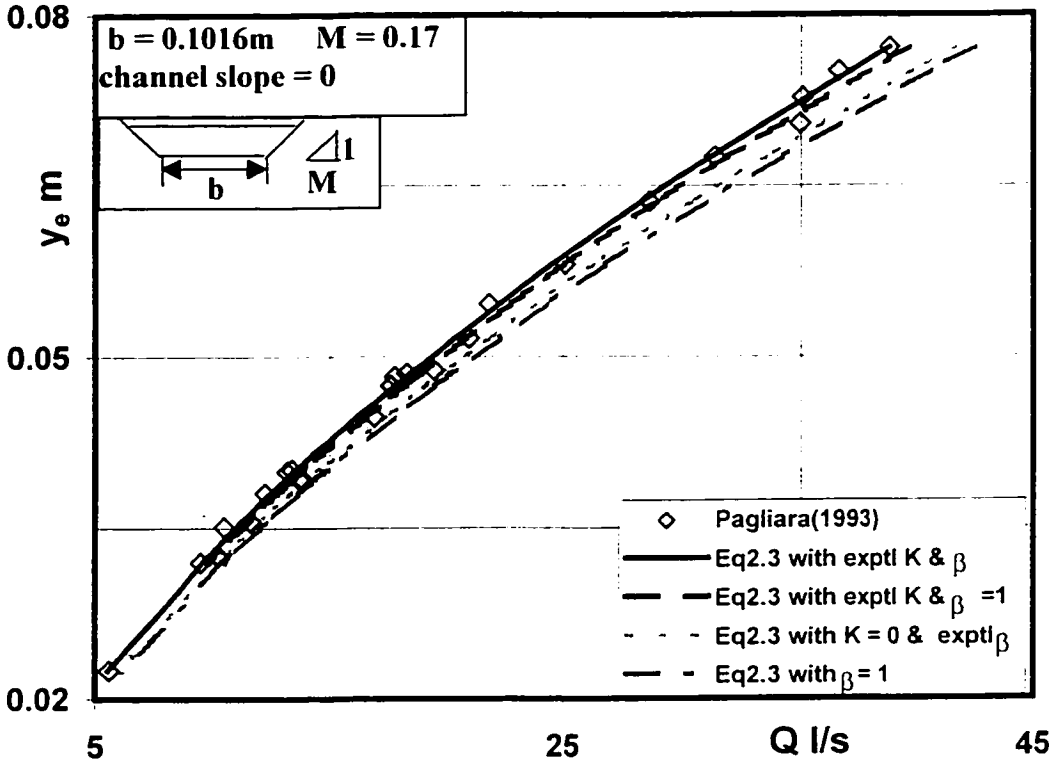

Fig 2.18 Discharge versus End Depth [(Pagliara 1993) Experiment]

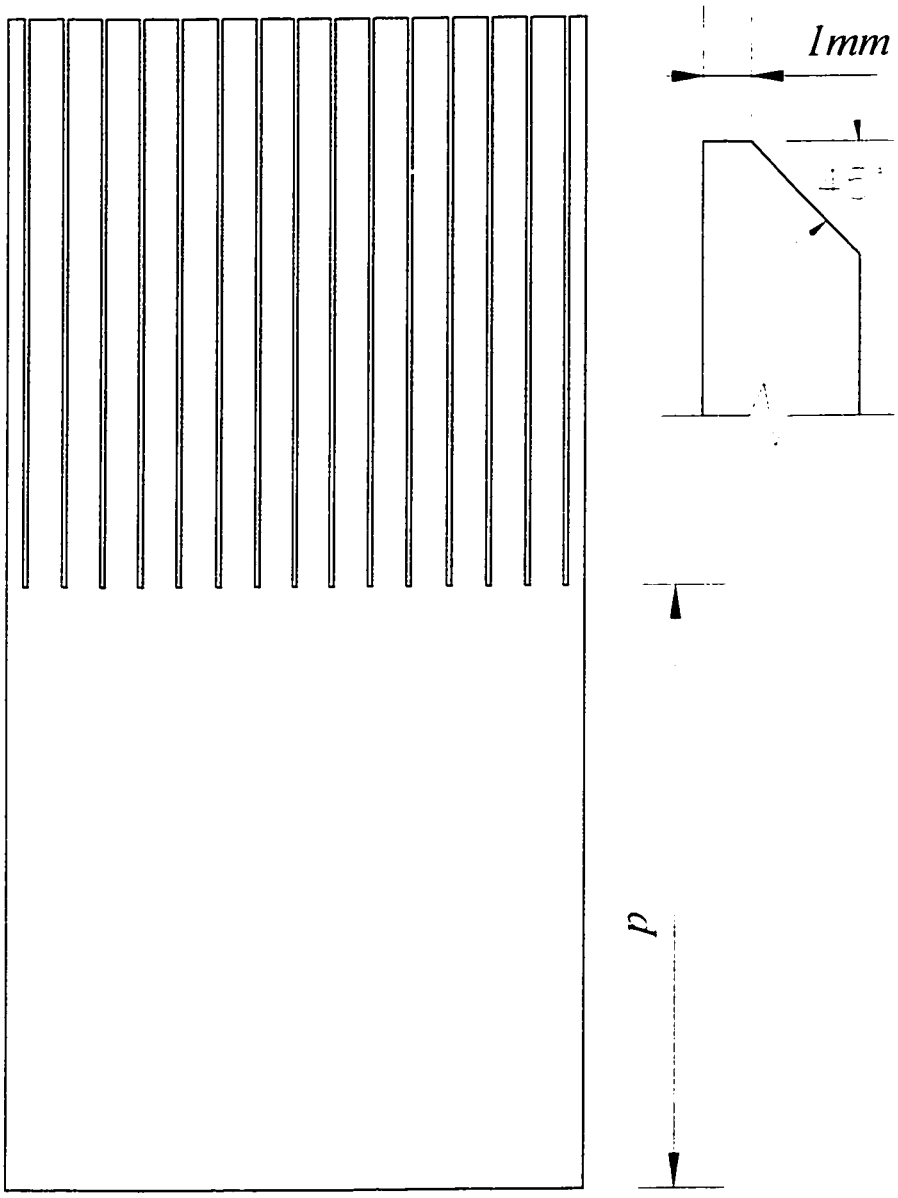

Fig.3.1 15 Multislit Weir and Weir Crest Detail

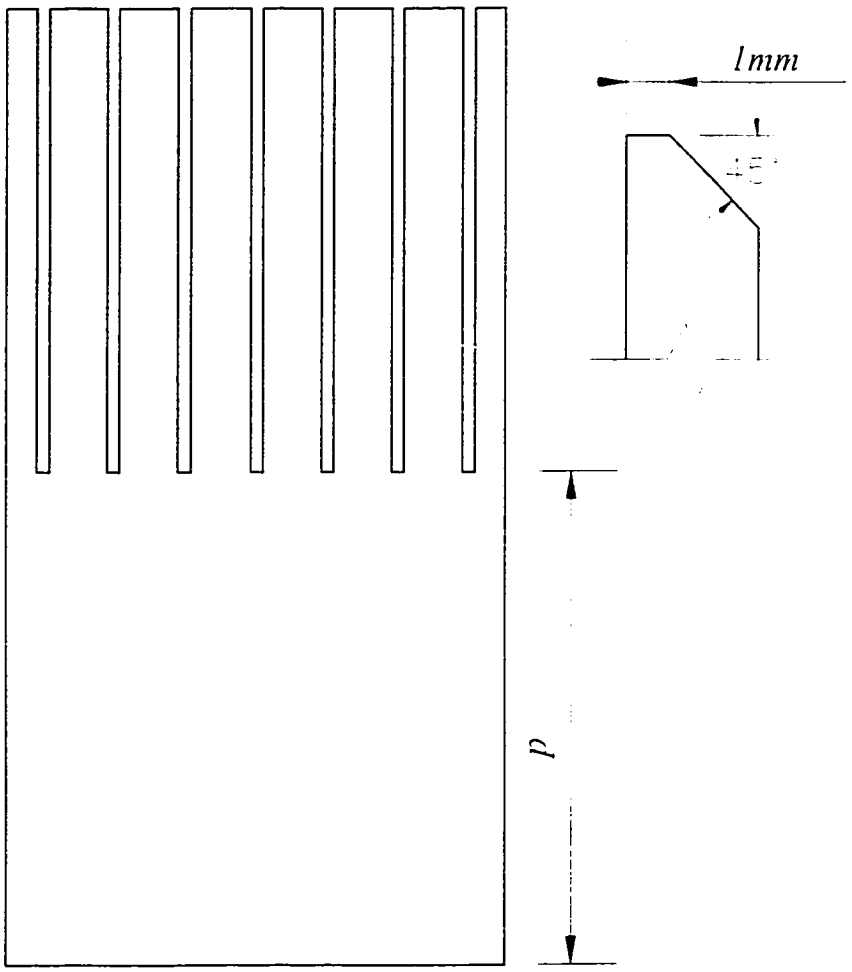

Fig.3.2 7 Multislit Weir and Weir Crest Detail

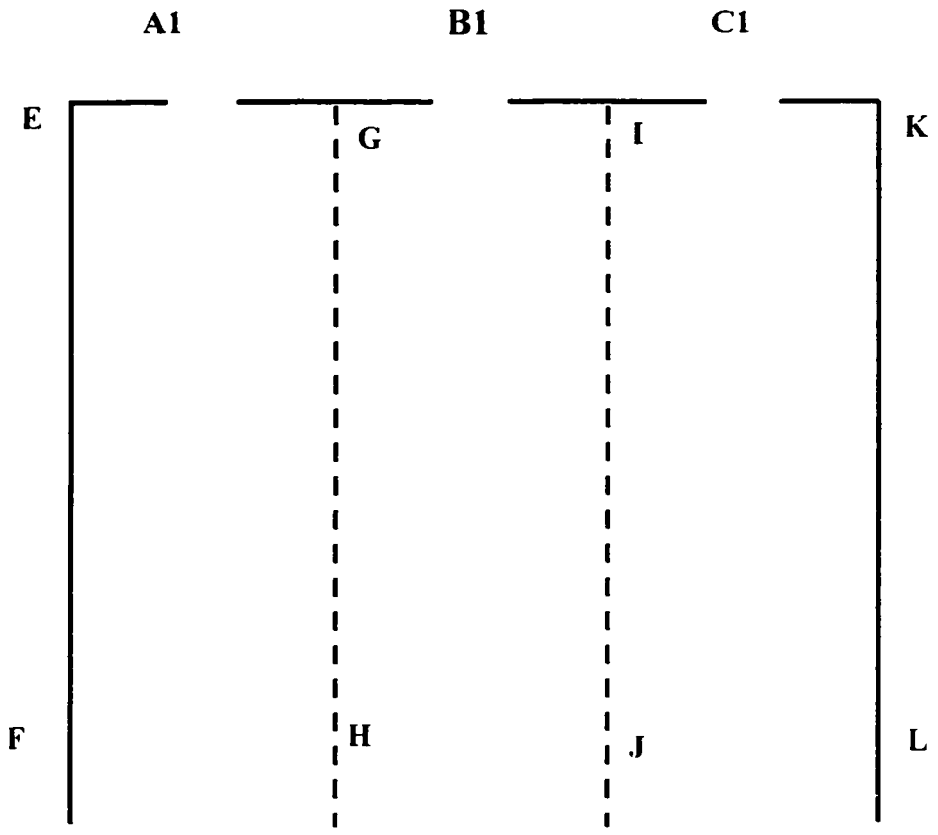

Fig.3.3 Stagnation streamlines distribution in 3 slit weir channel

All dimension in: mm

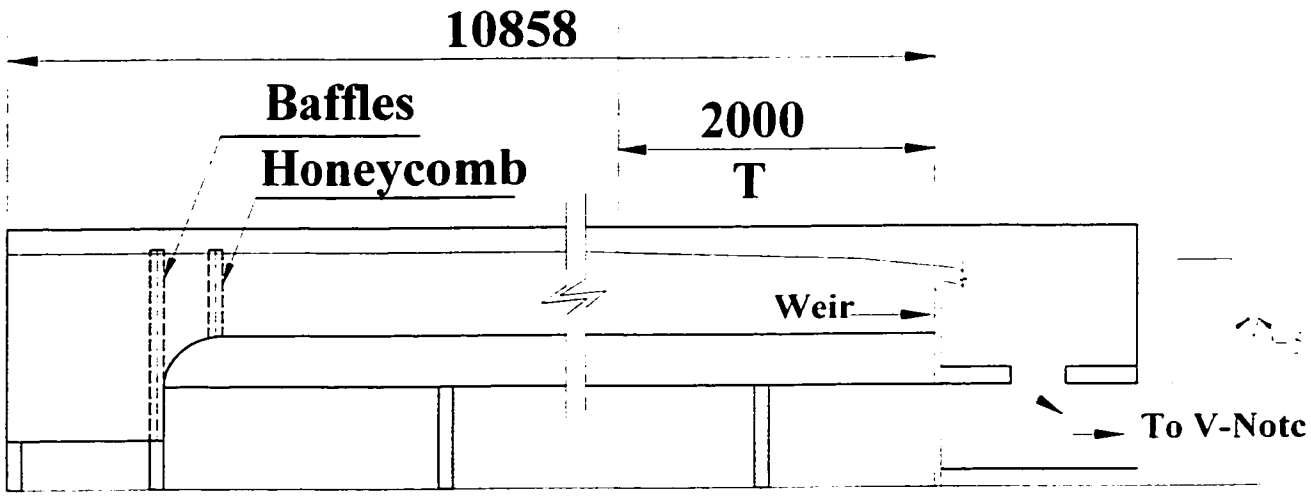

T: Measuring Section

Fig 3.4 Experiment Set-up (channel 1) for Multislit weir study

All dimension in: mm

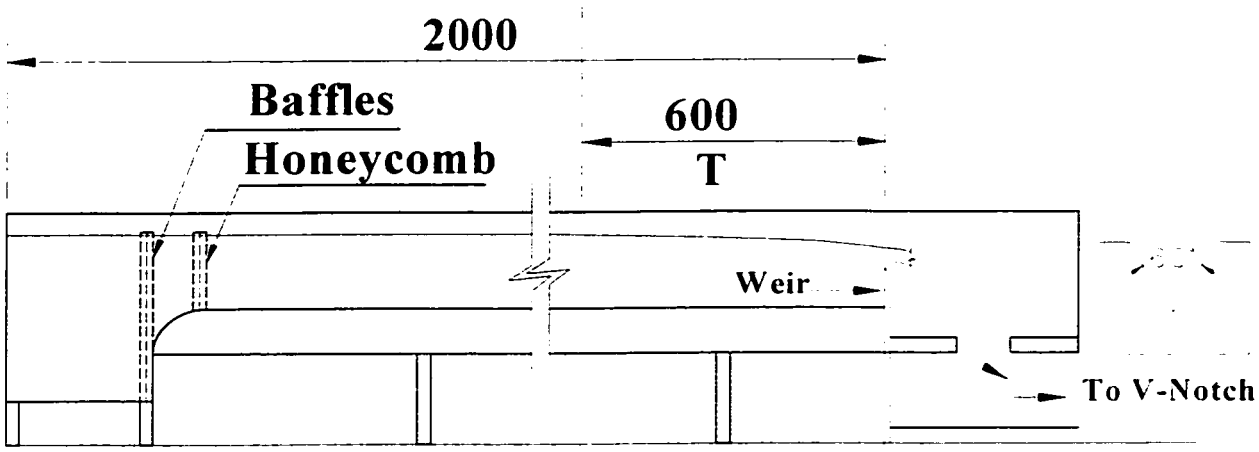

T: Measuring Section

Fig 3.5 Experiment Set-up (channel 2) for Multislit weir study

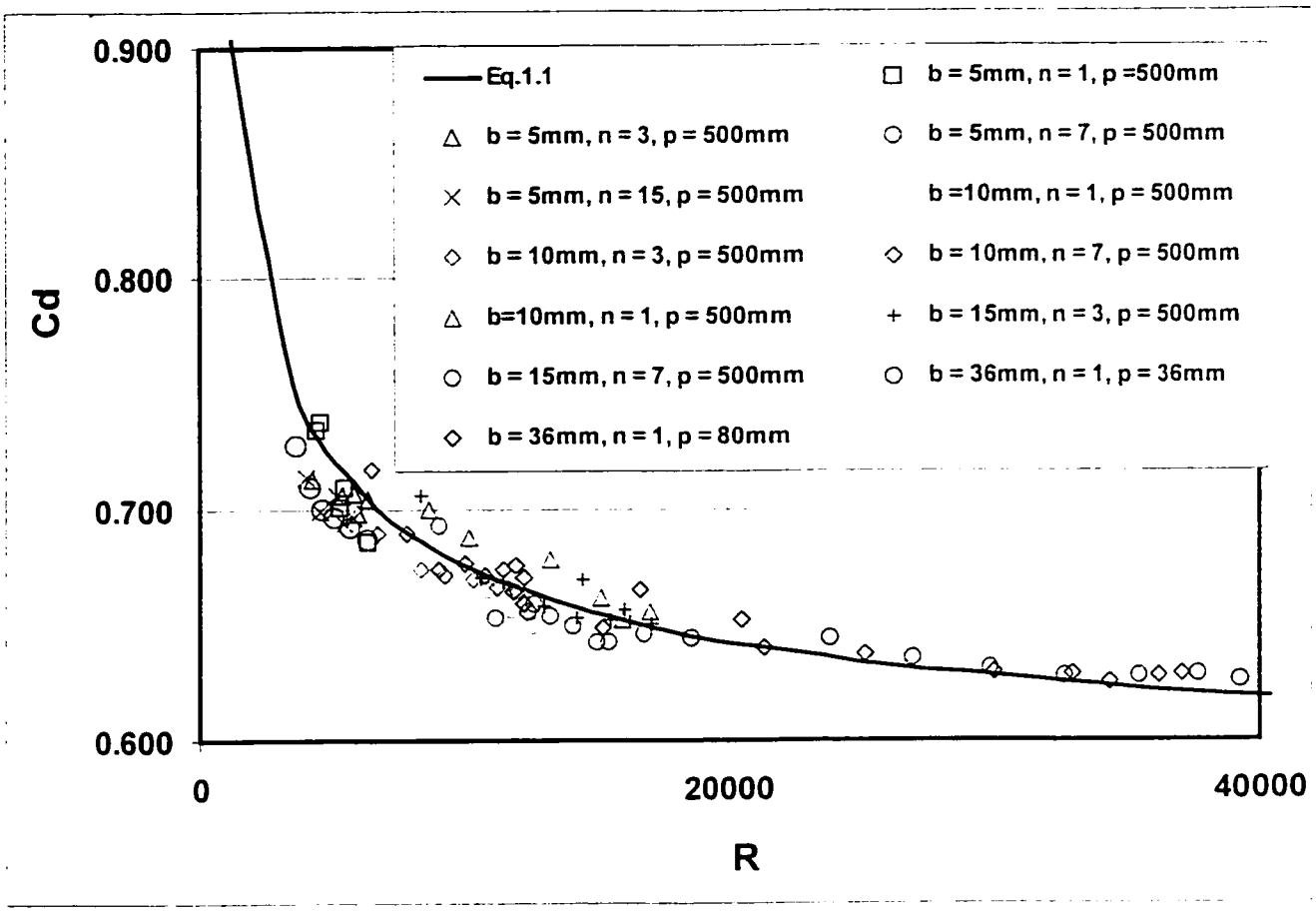

Fig 3.6 Discharge Coefficient versus Reynolds Number

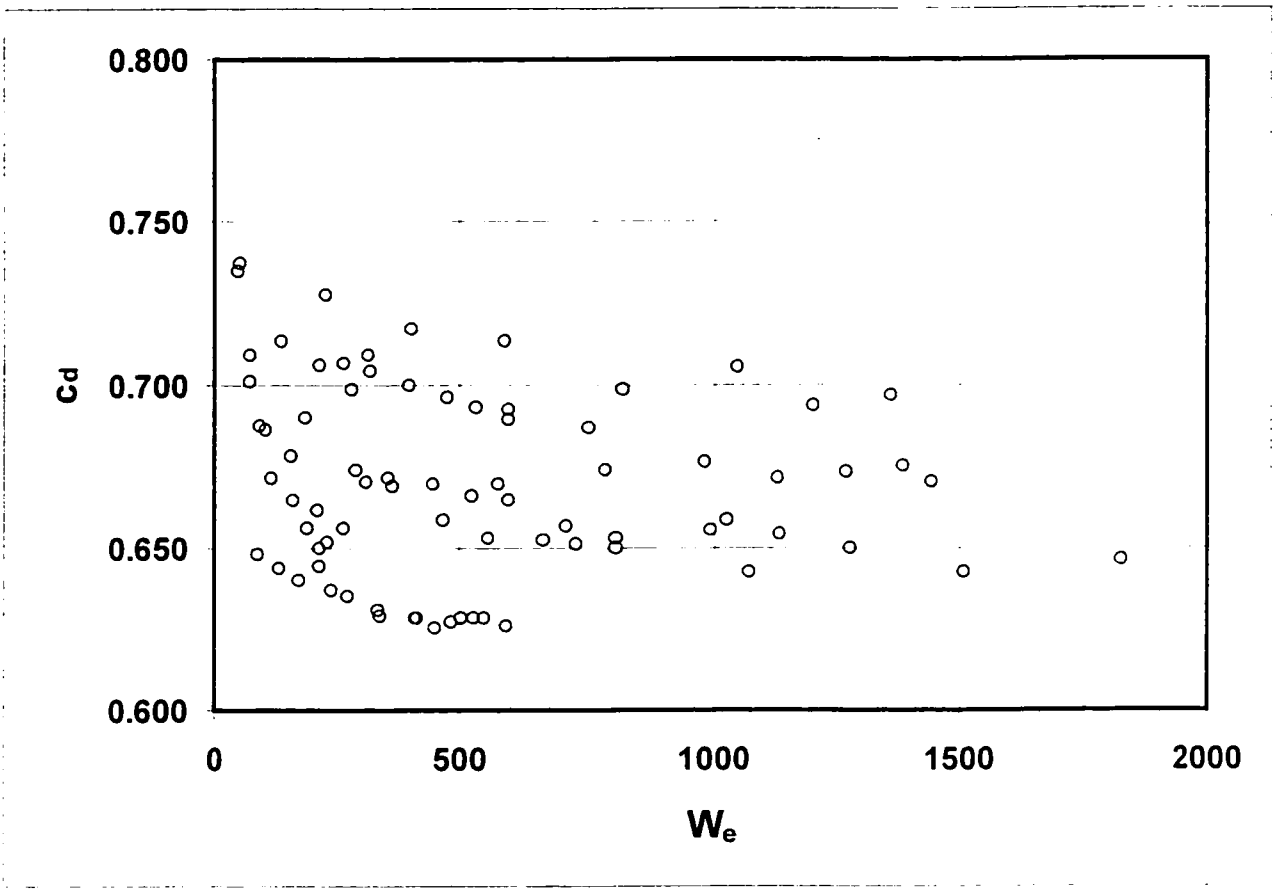

Fig 3.7 Discharge Coefficient versus W_e

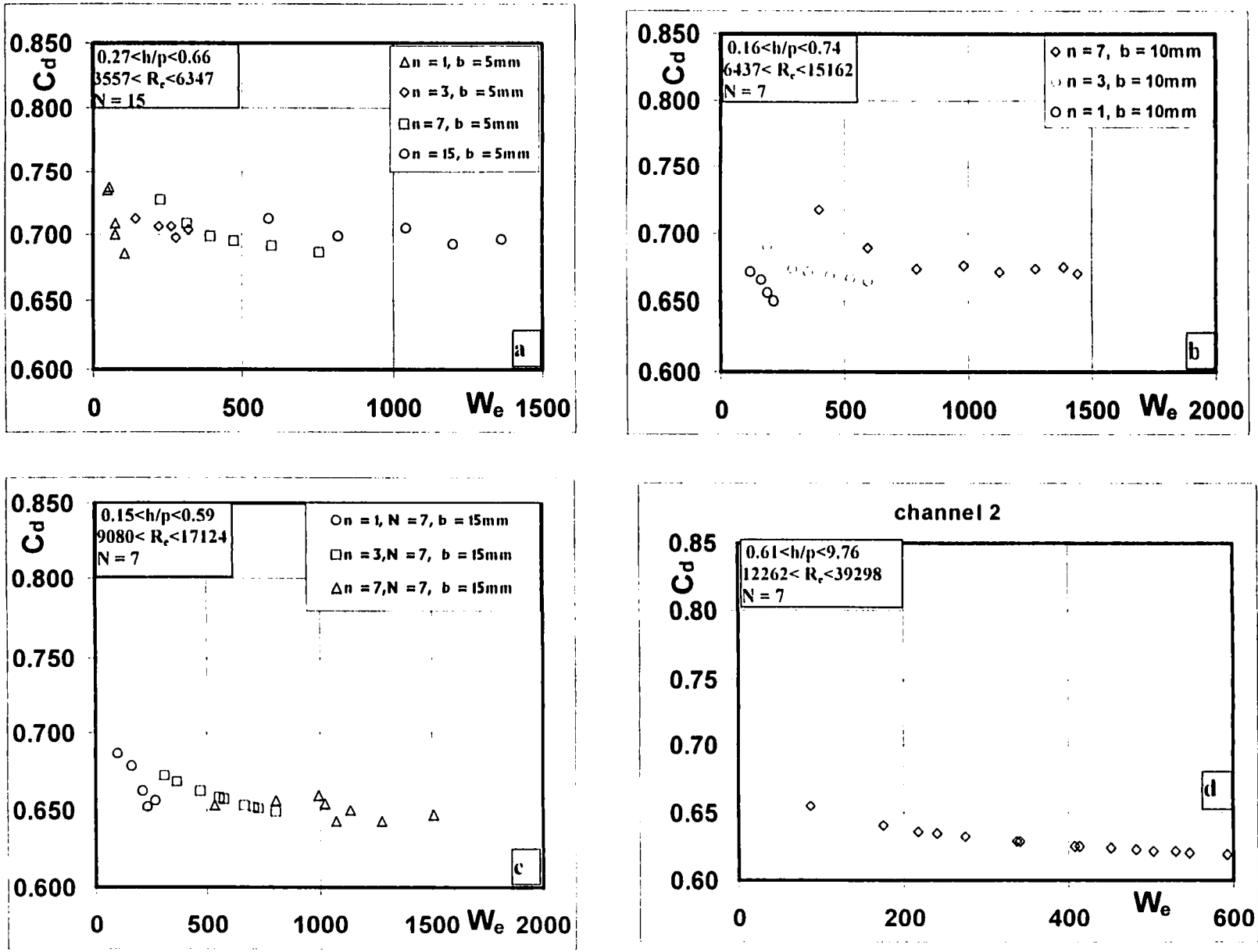

Fig 4.3 Discharge Coefficient versus W_e

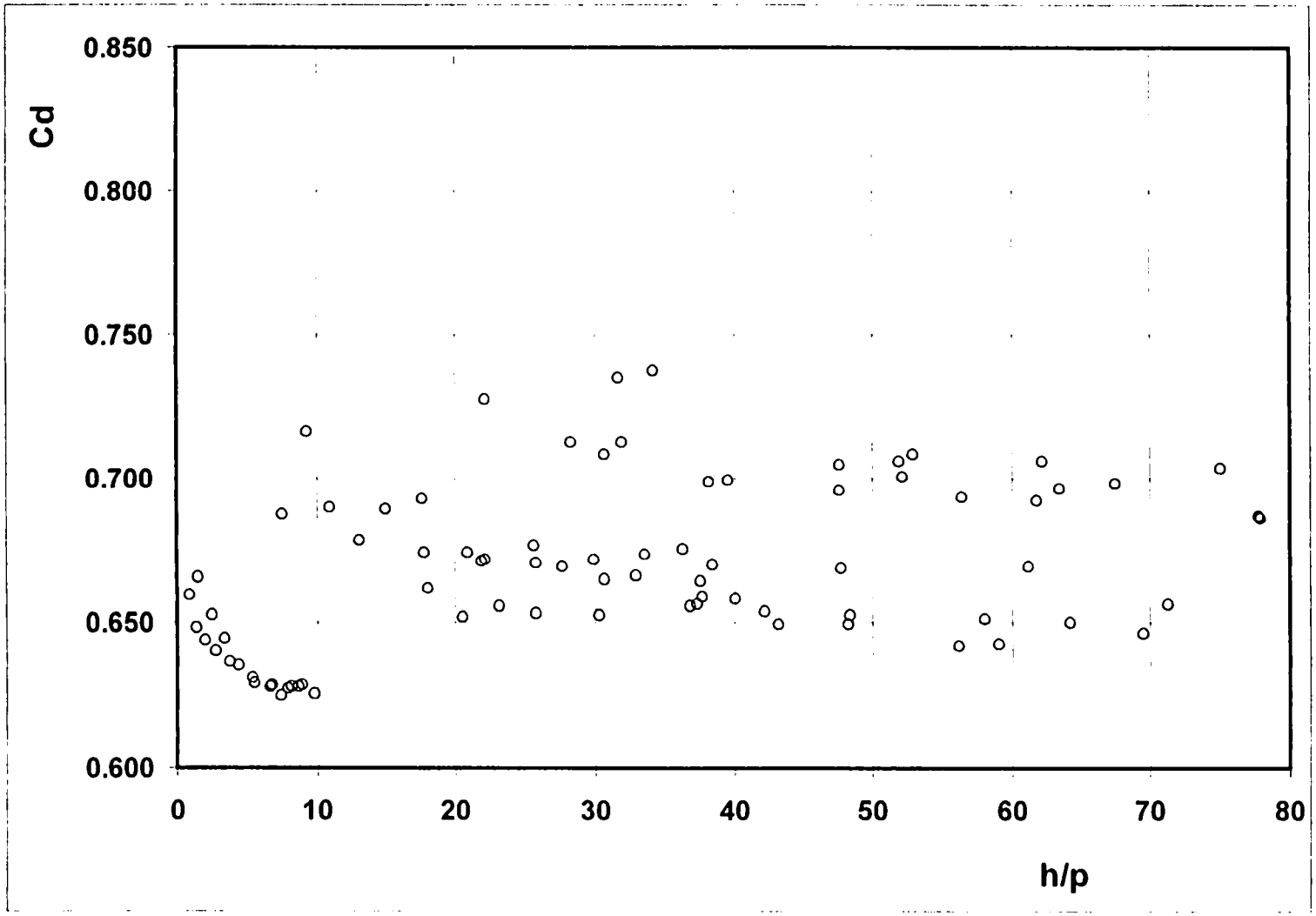

Fig 3.9 Discharge Coefficient versus h/p

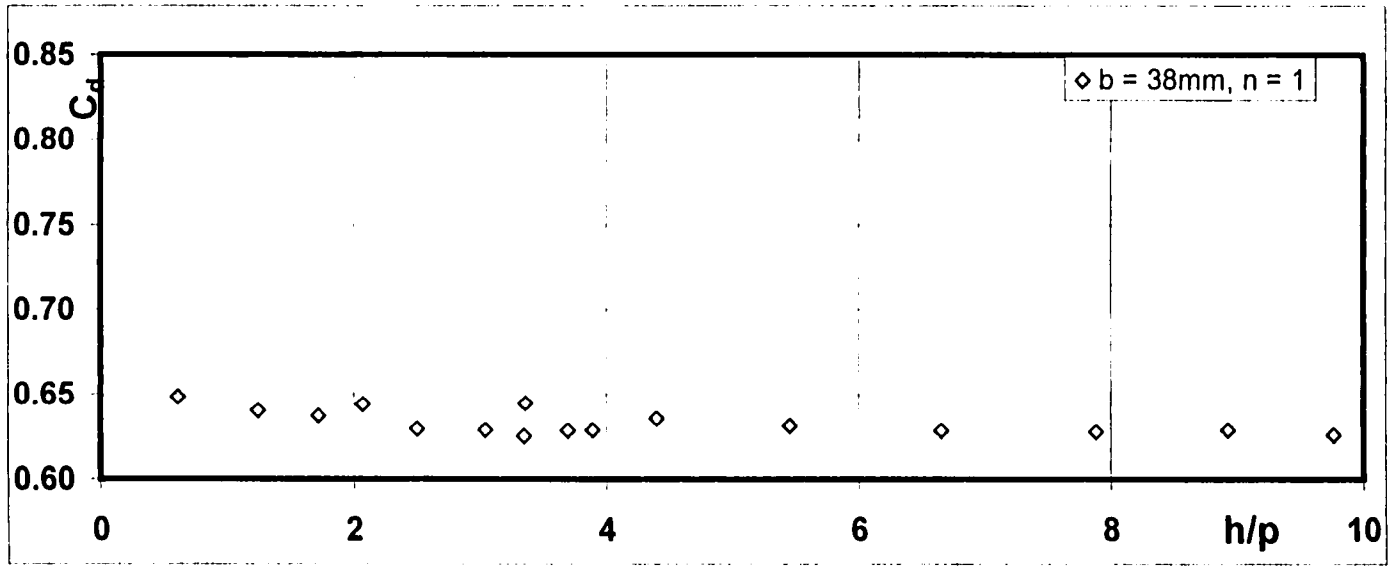

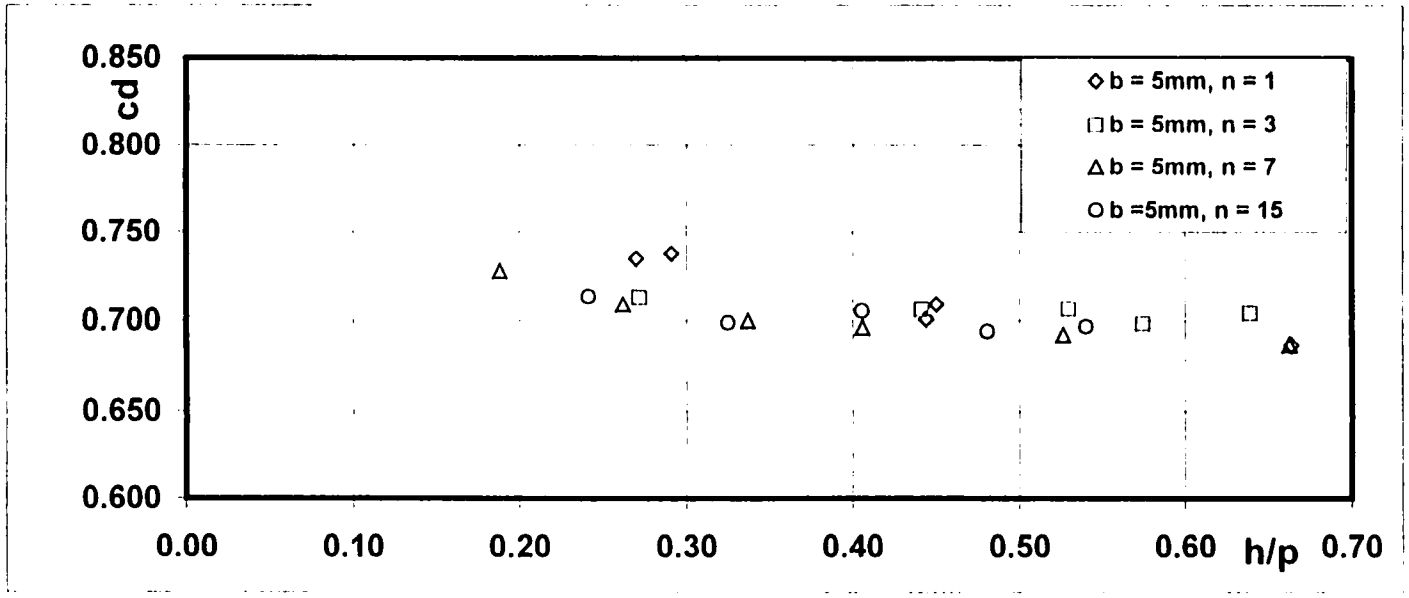

Fig 3.10 Discharge Coefficient versus h/p

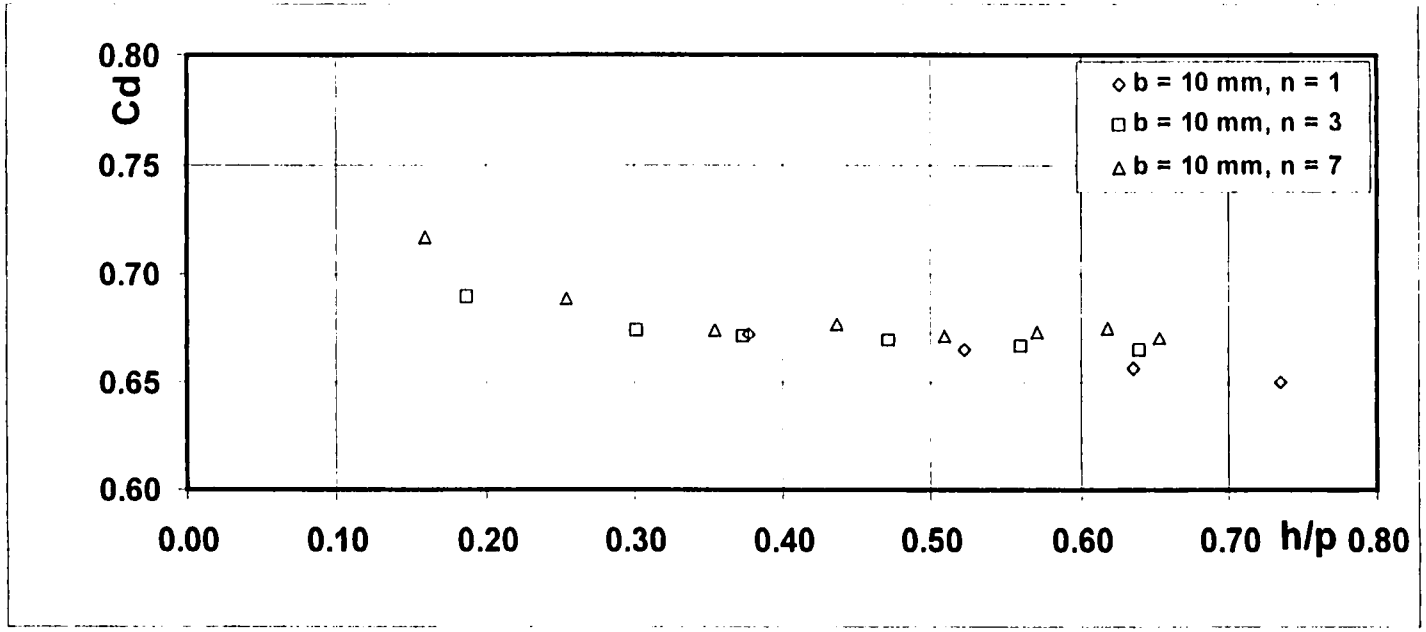

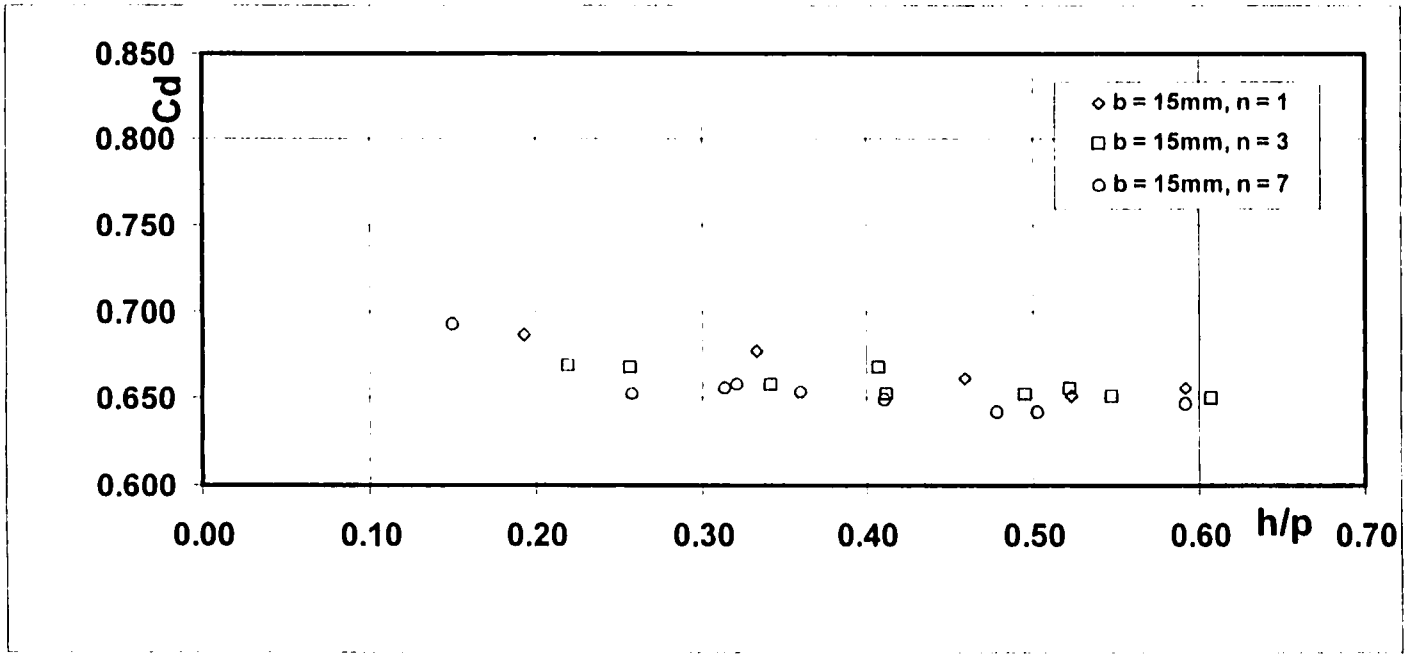

Fig 3.11 Discharge Coefficient versus h/p

Appendix B: Tabulation of data

Q=17.9l/s
y_e=74.8mm x=0

Depth	section A	section B	section C	section D
Z (mm)	Pressure head h_A(mm)	Pressure head h_B(mm)	Pressure head h_C(mm)	Pressure head h_D(mm)
0	0	0	0	
1.5	12.3	13.2	14	
4	15.8	16.3	17.4	
10	18.8	19.8	19.7	
15	19.9	20.1	20.2	
20	19.8	20	20.2	
25	19.5	20.1	19.5	
30	19.4	19	18.4	0
40	15.9	15.7	15.5	14.1
50	11.8	11.2	11.6	10.8
60	6.6	6.8	7.1	7.6
70	2.5	3.2	3.6	3.6
74.8	0	0	0	0

Table 2.1 Pressure Head and Coefficient Distribution at End Depth

Q=17.9l/s
y_e=74.8mm x=0

z mm	u m/s	v m/s	b m	α
0	0	1	0.127	1.025
1.5	1.338	1.1690	0.13	
5	1.354	1.2615	0.137	
10	1.403	1.3323	0.147	β
15	1.363	1.3476	0.157	1.015
20	1.376	1.3618	0.167	
25	1.292	1.3269	0.177	
30	1.288	1.3075	0.187	
40	1.258	1.2827	0.207	
50	1.218	1.2504	0.227	
60	1.196	1.2232	0.247	
70	1.172	1.1976	0.267	
74.8	1.160	1.179	0.277	

Table 2.2 Determination of Energy Coefficient α and Momentum Coefficient β

Q=19.5l/s

Y_e=78.6mm x=15mm

Z mm	u m/s	$d\psi$ m^2/s	ψ m^2/s
0	0	0	0
1.5	1.24	0.002	0.002
5	1.313	0.005	0.006
10	1.35	0.007	0.013
15	1.35	0.007	0.020
20	1.361	0.007	0.027
25	1.355	0.007	0.034
30	1.34	0.007	0.040
40	1.304	0.013	0.053
50	1.242	0.012	0.066
60	1.215	0.012	0.078
70	1.169	0.012	0.090
75	1.166	0.006	0.095
77	1.162	0.002	0.098

Table 2.3 Streamline Distribution at x=15mm Section

Z mm	u m/s	$d\psi$ m^2/s	ψ m^2/s
0	0	0	0
1.5	0.8960	0.0013	0.0013
5	1.0450	0.0037	0.0050
10	1.1140	0.0056	0.0106
15	1.1600	0.0058	0.0164
20	1.1860	0.0059	0.0223
25	1.2080	0.0060	0.0283
30	1.2250	0.0061	0.0345
40	1.2170	0.0122	0.0466
50	1.1840	0.0118	0.0585
60	1.1730	0.0117	0.0702
70	1.1560	0.0116	0.0818
75	1.1310	0.0057	0.0874
77	1.1460	0.0023	0.0897
79	1.1320	0.0023	0.0920
81	1.1300	0.0023	0.0942
83	1.0860	0.0022	0.0964
85	1.0840	0.0022	0.0986

Table 2.4 Streamline Distribution at x=60mm Section

Z mm	u m/s	$d\psi$ m^2/s	ψ m^2/s
0	0	0	0
1.5	0.8050	0.0012	0.0012
5	0.9930	0.0035	0.0047
10	0.9970	0.0050	0.0097
15	1.0480	0.0052	0.0149
20	1.0650	0.0053	0.0202
25	1.1120	0.0056	0.0258
30	1.1270	0.0056	0.0314
40	1.1300	0.0113	0.0427
50	1.1270	0.0113	0.0540
60	1.1290	0.0113	0.0653
70	1.1080	0.0111	0.0764
75	1.1040	0.0055	0.0819
77	1.1060	0.0022	0.0841
79	1.0800	0.0022	0.0863
81	1.1060	0.0022	0.0885
83	1.0820	0.0022	0.0906
85	1.0840	0.0022	0.0928
87	1.08	0.0022	0.0950
92	0.746	0.0037	0.0987

Table 2.5 Streamline Distribution at x=120mm Section

streamline	streamline curvature radius	pressure correction	theoretical pressure head	lab pressure head
m^2/s	m	m	m	m
$\psi 1$	0.521	0.000	0.0001	0.0002
$\psi 2$	0.506	0.007	0.0128	0.0122
$\psi 3$	0.459	0.014	0.0187	0.0184
$\psi 4$	0.424	0.028	0.0239	0.0210
$\psi 5$	0.356	0.043	0.0187	0.0190

Table 2.6 Comparisons Between Theoretical Pressure Head and Lab Pressure Head

Q=17.9l/s

Y_e=74.5mm x=15mm

depth	*u*	*w*	*vw*	*v*	static pressure	total energy	energy different ratio
mm	m/s	m/s	m/s	m/s	cm	m	
0	1.162	0.08	0.166	0.1455			
1.5	1.236	0.09	0.16	0.1323	18.89	0.268	*3.843*
5	*1.287*	*0.09*	*0.155*	*0.1262*	*18.89*	*0.275*	*1.537*
10	1.318	0.097	0.152	0.1170	18.94	0.279	*-0.090*
15	1.317	0.099	0.151	0.1140	19.05	0.280	*-0.428*
20	1.332	0.091	0.148	0.1167	19.19	0.283	*-1.631*
25	1.287	0.09	0.142	0.1098	19.34	0.279	*0.005*
30	1.277	0.084	0.139	0.1107	19.52	0.279	*-0.155*
40	1.253	0.082	0.135	0.1072	19.89	0.280	*-0.350*
50	1.227	0.073	0.11	0.0823	20.31	0.280	*-0.563*
60	1.226	0.076	0.107	0.0753	20.67	0.284	*-1.788*
70	1.168	0.074	0.106	0.0759	21.09	0.281	*-0.759*

Table 2.7 Total Energy at Section H

Q=17.9l/s
Y_c=74.5mm x=30mm

depth	*u*	*w*	*vw*	*v*	static pressure	total energy	energy different ratio
mm	m/s	m/s	m/s	m/s	cm	m	
0	1.059	0.046	0.148	0.1407			
1.5	1.134	0.058	0.1332	0.1199	20.35	0.270	*6.490*
5	*1.22*	*0.07*	*0.12879*	*0.1081*	*20.35*	*0.280*	*2.914*
10	1.233	0.072	0.12456	0.1016	20.35	0.282	*2.366*
15	1.271	0.071	0.12033	0.0972	20.35	0.287	*0.694*
20	1.288	0.07	0.1032	0.0758	20.35	0.289	*-0.011*
25	1.282	0.06	0.09944	0.0793	20.4	0.288	*0.102*
30	1.266	0.058	0.09568	0.0761	20.45	0.287	*0.665*
40	1.248	0.04	0.08816	0.0786	20.65	0.286	*0.797*
50	1.236	0.053	0.08064	0.0608	20.86	0.287	*0.618*
60	1.256	0.057	0.07312	0.0458	21.12	0.292	*-1.153*
70	1.194	0.064	0.0738	0.0367	21.38	0.287	*0.638*

Table 2.8 Total Energy at Section I

Q=17.9l/s
Y_c=74.5mm x=60mm

depth	*u*	*w*	*vw*	*v*	static pressure	total energy	energy different ratio
mm	m/s	m/s	m/s	m/s	cm	m	
0	0.89	0.062	0.113	0.0945	21.36	0.255	
1.5	0.975	0.066	0.11	0.0880	21.36	0.263	9.491
5	1.045	0.08	0.108	0.0726	21.36	0.270	7.003
10	1.094	0.083	0.106	0.0659	21.36	0.275	5.160
15	*1.135*	*0.086*	*0.105*	*0.0602*	*21.36*	*0.280*	3.550
20	1.166	0.086	0.105	0.0602	21.36	0.283	2.291
25	1.174	0.083	0.098	0.0521	21.41	0.285	1.812
30	1.202	0.079	0.094	0.0509	21.48	0.289	0.409
40	1.206	0.076	0.085	0.0381	21.56	0.290	-0.010
50	1.185	0.068	0.08	0.0421	21.69	0.289	0.441
60	1.178	0.058	0.075	0.0475	21.89	0.290	0.054
70	1.161	0.068	0.077	0.0361	21.99	0.289	0.405

Table 2.9 Total Energy at Section J

Present experiment :b=0.127m, m=1,k=0.27.velocity coefficient=1.015						
y_c m	Q l/s	Q predicted with β & K (l/s)	% deviation with exptl. β & K	% deviation with exptl. K & $\beta = 1$	% deviation only with exptl. β	% deviation with $\beta = 1$ & $K = 0$
0.08	21.35	21.19	0.75	-1.40	-6.57	-8.66
0.077	19.74	19.78	-0.18	-2.35	-7.56	-9.68
0.0764	19.63	19.50	0.66	-1.49	-6.66	-8.76
0.0761	19.69	19.36	1.68	-0.45	-5.56	-7.64
0.0748	18.59	18.77	-0.97	-3.16	-8.41	-10.55
0.0739	18.53	18.37	0.87	-1.28	-6.43	-8.53
0.072	18.45	17.53	5.00	2.93	-2.00	-4.02
0.0704	16.99	16.84	0.90	-1.26	-6.40	-8.50
0.065	14.85	14.62	1.58	-0.57	-5.66	-7.76
0.0609	13.23	13.03	1.49	-0.67	-5.75	-7.86
0.0576	11.87	11.83	0.41	-1.78	-6.90	-9.04
0.0529	10.23	10.20	0.29	-1.91	-7.03	-9.18
0.0446	7.51	7.62	-1.46	-3.72	-8.89	-11.09
0.0397	6.24	6.27	-0.42	-2.68	-7.77	-9.97

Table 2.10 Dependence of Predicting Discharge on Coefficient β & K

Rajaratnam's experiment: b=0.1016m, m=0.17, k=0.27.velocity coefficient=1.015						
y_c m	Q l/s	Q predicted with β & K (l/s)	% deviation with exptl. β & K	% deviation with exptl. K & $\beta = 1$	% deviation only with exptl. β	% deviation with $\beta = 1$ & $K = 0$
0.1619	41.10	40.35	1.83	-0.39	-5.29	-7.45
0.1509	37.14	35.94	3.23	1.03	-3.79	-5.92
0.147	35.01	34.40	1.75	-0.48	-5.37	-7.54
0.1399	30.09	31.75	-5.54	-7.94	-13.18	-15.52
0.1284	27.91	27.58	1.16	-1.10	-6.00	-8.20
0.1241	25.53	26.11	-2.27	-4.62	-9.68	-11.96
0.1061	19.73	20.28	-2.81	-5.19	-10.27	-12.58
0.0927	16.81	16.34	2.81	0.55	-4.25	-6.45
0.0817	13.16	13.37	-1.61	-4.00	-9.01	-11.32
0.0744	11.32	11.53	-1.82	-4.23	-9.25	-11.59
0.0494	5.97	6.05	-1.31	-3.77	-8.86	-11.25
0.039	4.10	4.18	-1.75	-4.27	-9.52	-11.96
0.0296	2.83	2.69	5.12	2.68	-2.54	-4.88

Table 2.11 Dependence of Predicting Discharge on Coefficient β & K

Keller's Experiment :b=0.15m, m=1,k=0.27.velocity coefficient=1.015						
y_c m	Q l/s	Q predicted with β & K (l/s)	% deviation with exptl. β & K	% deviation with exptl. K & $\beta = 1$	% deviation only with exptl. β	% deviation with $\beta = 1$ & $K = 0$
0.0779	23.19	22.74	1.94	-0.20	-5.28	-7.36
0.0758	22.16	21.67	2.21	0.08	-4.98	-7.06
0.0741	21.20	20.82	1.79	-0.36	-5.43	-7.53
0.0712	21.03	19.41	7.69	5.66	0.91	-1.07
0.0711	20.93	19.37	7.47	5.44	0.68	-1.30
0.0699	19.20	18.80	2.09	-0.05	-5.10	-7.19
0.0694	19.12	18.56	2.91	0.78	-4.22	-6.30
0.0691	19.26	18.42	4.34	2.24	-2.69	-4.73
0.0683	19.15	18.05	5.72	3.65	-1.20	-3.22
0.0682	18.99	18.01	5.17	3.09	-1.79	-3.82
0.0678	19.30	17.82	7.64	5.61	0.86	-1.12
0.0673	18.45	17.60	4.62	2.53	-2.38	-4.42
0.0662	17.63	17.10	3.00	0.87	-4.11	-6.19
0.0647	17.33	16.43	5.17	3.08	-1.79	-3.83
0.0645	17.29	16.35	5.46	3.37	-1.48	-3.51
0.0641	17.95	16.17	9.91	7.92	3.30	1.36
0.0631	16.61	15.74	5.25	3.16	-1.70	-3.74
0.0618	15.97	15.18	4.92	2.82	-2.05	-4.10
0.0616	15.96	15.10	5.39	3.30	-1.55	-3.58
0.0612	16.14	14.93	7.49	5.45	0.71	-1.28
0.061	17.09	14.85	13.12	11.20	6.75	4.88
0.0605	14.79	14.64	1.02	-1.17	-6.23	-8.36
0.0601	15.21	14.47	4.85	2.74	-2.13	-4.18
0.0595	14.58	14.23	2.43	0.27	-4.72	-6.83
0.0588	14.64	13.94	4.78	2.67	-2.20	-4.25
0.0576	13.69	13.46	1.70	-0.48	-5.50	-7.63
0.0575	14.44	13.42	7.08	5.02	0.27	-1.73
0.056	13.46	12.83	4.71	2.60	-2.27	-4.33
0.0547	12.30	12.32	-0.19	-2.42	-7.53	-9.70
0.054	12.47	12.06	3.31	1.16	-3.77	-5.86
0.0538	12.37	11.98	3.14	0.99	-3.95	-6.05

Table 2.12 Dependence of Predicting Discharge on Coefficient β & K

Diskin's Experiment :b=0.167m, m=1.5,k=0.27.velocity coefficient=1.015						
y_c m	Q l/s	Q predicted with β & K (l/s)	% deviation with exptl. β & K	% deviation with exptl. K & $\beta = 1$	% deviation only with exptl. β	% deviation with $\beta = 1$ & $K = 0$
0.0829	31.95	31.09	2.69	0.60	-4.51	-6.55
0.078	28.32	27.80	1.86	-0.26	-5.39	-7.46
0.0741	25.64	25.27	1.44	-0.69	-5.84	-7.92
0.068	22.38	21.62	3.40	1.31	-3.73	-5.77
0.064	20.03	19.41	3.12	1.02	-4.02	-6.07
0.0619	18.99	18.27	3.79	1.70	-3.30	-5.34
0.0579	16.78	16.24	3.21	1.10	-3.91	-5.97
0.0509	13.21	12.95	2.01	-0.14	-5.19	-7.29
0.0451	10.58	10.51	0.72	-1.47	-6.56	-8.70
0.0399	8.72	8.53	2.13	-0.05	-5.05	-7.16

Table 2.13 Dependence of Predicting Discharge on Coefficient β & K

Stefano and Viti"s Experiment :b=0.30m, m=1,k=0.27.velocity coefficient=1.015						
y_c m	Q l/s	Q predicted with exptl β & K (l/s)	% deviation with exptl. β & K	% deviation with exptl . K & $\beta = 1$	% deviation only with exptl. β	% deviation with $\beta = 1$ & $K = 0$
0.0771	38.85	38.85	0.00	-2.27	-7.30	-9.50
0.075	36.60	37.13	-1.44	-3.74	-8.84	-11.08
0.0727	35.05	35.28	-0.66	-2.95	-8.00	-10.22
0.0704	34.95	33.47	4.22	2.04	-2.76	-4.88
0.0675	31.42	31.26	0.52	-1.75	-6.73	-8.93
0.0636	28.70	28.38	1.12	-1.14	-6.08	-8.28
0.0581	25.11	24.52	2.35	0.10	-4.76	-6.94
0.0546	21.72	22.19	-2.17	-4.53	-9.60	-11.89
0.0516	20.85	20.27	2.77	0.52	-4.30	-6.49
0.0488	19.38	18.55	4.31	2.08	-2.65	-4.81
0.0485	18.20	18.36	-0.90	-3.25	-8.24	-10.52
0.0482	17.70	18.18	-2.73	-5.12	-10.21	-12.52
0.0474	17.50	17.71	-1.18	-3.53	-8.53	-10.82
0.0474	17.52	17.71	-1.06	-3.41	-8.41	-10.69
0.0447	16.81	16.13	4.03	1.80	-2.94	-5.12
0.0401	13.40	13.59	-1.40	-3.78	-8.77	-11.08
0.0399	13.20	13.48	-2.13	-4.52	-9.55	-11.88
0.0393	13.82	13.16	4.75	2.52	-2.17	-4.34
0.039	13.84	13.01	6.03	3.83	-0.80	-2.94
0.038	12.25	12.48	-1.92	-4.31	-9.32	-11.65
0.0355	11.64	11.22	3.61	1.34	-3.39	-5.60
0.0351	10.50	11.02	-4.97	-7.44	-12.60	-15.00
0.0326	10.21	9.82	3.83	1.56	-3.16	-5.37
0.032	9.45	9.54	-0.93	-3.32	-8.26	-10.59
0.0225	5.58	5.52	1.06	-1.32	-6.15	-8.45

Table 2.14 Dependence of Predicting Discharge on Coefficient β & K

Number of weirs in unit	Weir Width	Effective Channel Width	Weir Height
	b mm	B mm	P mm
1 of 1	*36*	*25.4*	*36*
1 of 1	*36*	*25.4*	*80*
1 of 15	5	600	587
1 of 7	10	600	587
1 of 7	15	600	587
3 of 15	5	200	587
3 of 7	10	200	587
3 of 7	15	200	587
7 of 15	5	85.7	587
7 of 7	10	85.7	587
7 of 7	15	85.7	587
15 of 15	5	40	587

Table 3.1 Multislit Weir Variable Range

Note 1:Numbers in italics (rows 1 and 2) of table 1-1 refer to tests in the flume for which B=300 mm.
Note 2:Last row of Table 1-1 indicates that 15 slits of 5 mm in the 15 slit unit are functioning.

Dimensionless Variable	Minimum Value	Maximum Value
R	3432	39299
W	46.6	1821.5
h/b	0.86	71.22
b/B	0.0083	0.125
h/P	0.12	9.8

Table 3.2 Dimensionless Variable Range

No.	Slit Number	Slit Width (m)	b/B	h/P	h/b	Re	W	Cd (ex.)
1	1	0.005	0.0083	0.27	31.66	4303	47.5	0.735
2	1	0.005	0.0083	0.29	34.16	4486	51.5	0.738
3	1	0.005	0.0083	0.44	52.16	5267	73.1	0.701
4	1	0.005	0.0083	0.66	77.90	6302	105.7	0.686
5	1	0.005	0.0083	0.45	52.88	5366	74.2	0.709
6	1	0.010	0.0167	0.38	22.10	9293	119.3	0.672
7	1	0.010	0.0167	0.52	30.70	10842	162.4	0.665
8	1	0.010	0.0167	0.64	37.29	11796	192.2	0.656
9	1	0.010	0.0167	0.74	43.20	12570	218.3	0.650
11	1	0.015	0.0250	0.46	17.95	15163	211.7	0.662
12	1	0.015	0.0250	0.59	23.13	17055	267.9	0.656
13	1	0.015	0.0250	0.52	20.43	15936	233.9	0.652
14	1	0.015	0.0250	0.33	13.03	13241	158.6	0.678
15	1	0.015	0.0250	0.19	7.55	10213	96.1	0.687
16	3	0.005	0.0250	0.27	31.90	4191	139.8	0.713
17	3	0.005	0.0250	0.44	51.84	5291	218.4	0.706
18	3	0.005	0.0250	0.53	62.18	5798	264.0	0.707
19	3	0.005	0.0250	0.57	67.48	5969	280.4	0.698
20	3	0.005	0.0250	0.64	75.02	6347	318.1	0.704
21	3	0.01	0.0500	0.19	10.97	6723	187.3	0.690
22	3	0.01	0.0500	0.30	17.70	8344	288.6	0.674
23	3	0.01	0.0500	0.37	21.88	9241	353.9	0.671
24	3	0.01	0.0500	0.47	27.67	10363	445.1	0.669
25	3	0.01	0.0500	0.56	32.85	11235	523.1	0.666
26	3	0.01	0.0500	0.64	37.58	11989	595.7	0.664
28	3	0.015	0.0750	0.22	25.78	10623	311.8	0.670
29	3	0.015	0.0750	0.34	40.06	13006	467.4	0.658
30	3	0.015	0.0750	0.41	25.78	14183	555.8	0.653
31	3	0.015	0.0750	0.49	48.38	15520	665.5	0.652
32	3	0.015	0.0750	0.55	58.06	16289	733.1	0.651
33	3	0.015	0.0750	0.61	64.20	17124	810.2	0.650
34	3	0.015	0.0750	0.52	71.22	16029	709.9	0.656
35	3	0.015	0.0750	0.41	61.18	14442	576.3	0.669
36	3	0.015	0.0750	0.26	47.76	11469	363.4	0.669
37	7	0.005	0.0583	0.19	22.06	3557	227.8	0.728
38	7	0.005	0.0583	0.26	30.70	4088	313.8	0.709
39	7	0.005	0.0583	0.34	39.56	4581	395.7	0.700
40	7	0.005	0.0583	0.41	47.64	4999	472.4	0.696
41	7	0.005	0.0583	0.53	61.82	5662	596.4	0.692
42	7	0.005	0.0583	0.66	77.76	6301	754.9	0.687
43	7	0.01	0.1167	0.16	9.31	6437	400.7	0.717
44	7	0.01	0.1167	0.26	14.98	7850	595.9	0.689
45	7	0.01	0.1167	0.35	20.79	9046	791.4	0.674

46	7	0.01	0.1167	0.44	25.62	10074	981.4	0.676
47	7	0.01	0.1167	0.51	29.87	10799	1127.7	0.671
48	7	0.01	0.1167	0.57	33.50	11470	1272.3	0.673
49	7	0.01	0.1167	0.62	36.27	11969	1385.3	0.675
50	7	0.01	0.1167	0.65	38.37	12214	1442.7	0.670
51	7	0.015	0.1750	0.59	69.42	16809	1821.5	0.646
52	7	0.015	0.1750	0.50	58.98	15407	1510.1	0.643
53	7	0.015	0.1750	0.48	56.08	15015	1073.0	0.642
54	7	0.015	0.1750	0.41	48.22	14083	1278.5	0.650
55	7	0.015	0.1750	0.36	42.18	13262	1133.8	0.654
56	7	0.015	0.1750	0.32	37.70	12624	1027.4	0.659
57	7	0.015	0.1750	0.31	36.84	12424	995.2	0.656
58	7	0.015	0.1750	0.26	30.26	11211	810.3	0.653
59	7	0.015	0.1750	0.15	17.62	9080	531.6	0.693
60	15	0.005	0.1250	0.24	28.30	3949	589.9	0.713
61	15	0.005	0.1250	0.33	38.16	4492	820.5	0.699
62	15	0.005	0.1250	0.41	47.60	5065	1045.7	0.705
63	15	0.005	0.1250	0.48	56.44	5424	1200.9	0.694
64	15	0.005	0.1250	0.54	63.44	5774	1362.6	0.697
65	1	0.036	0.1181	2.07	2.07	18628	133.2	0.64
66	1	0.036	0.1181	3.36	3.36	23750	216.5	0.64
67	1	0.036	0.1181	4.39	4.39	26774	275.1	0.64
68	1	0.036	0.1181	5.45	5.45	29621	336.7	0.63
69	1	0.036	0.1181	6.65	6.65	32571	407.1	0.63
70	1	0.036	0.1181	7.88	7.88	35410	481.2	0.63
71	1	0.036	0.1181	8.93	8.93	37753	547.0	0.63
72	1	0.036	0.1181	9.76	9.76	39299	592.7	0.63
73	1	0.036	0.1181	0.61	1.36	15189	88.5	0.65
75	1	0.036	0.1181	1.24	2.76	21365	175.2	0.64
76	1	0.036	0.1181	1.72	3.82	25020	240.2	0.64
77	1	0.036	0.1181	2.50	5.56	29826	341.4	0.63
78	1	0.036	0.1181	3.04	6.76	32844	413.9	0.63
79	1	0.036	0.1181	3.35	7.44	34270	450.7	0.62
80	1	0.036	0.1181	3.69	8.21	36179	502.3	0.63
81	1	0.036	0.1181	3.89	8.64	37127	529.0	0.63

Table 3.3 Multislit test and analysis data